

Elastic waves in bearing raceways: the forward and inverse problem

Jessica J. Kent, Matheus de C. Loures, Art L. Gower¹

Department of Mechanical, Aerospace and Civil Engineering, The University of Sheffield, UK

December 20, 2024

Abstract

Turbines are crucial to our energy infrastructure, and ensuring their bearings function with minimal friction while often supporting heavy loads is vital. Vibrations within a bearing can signal the presence of defects, friction, or misalignment. However, current detection methods are neither robust nor easy to automate. We propose a more quantitative approach by modelling the elastic waves within bearing raceways. By approximating the raceway as a hollow cylinder, we derive straightforward 4x4 systems for its vibrational modes, enabling both forward and inverse problem-solving. We also demonstrate how to significantly reduce the number of required sensors by using a simple prior: the known number of rollers and their angular speed. We present numerical examples showcasing the full recovery of contact traction between bearings and the raceway, as well as the detection of elastic emissions.

1 Introduction

Bearings are essential parts of modern industrial machinery; found everywhere from bicycles to wind turbines to jet engines [13]. Their main purpose is to reduce friction and constrain the motion of rotating components; as such, their maintenance and efficiency remains an important industrial problem and an active field of study [14].

Current methods. The most successful methods to monitor the condition of roller bearings are based on vibration analysis: analysing the frequency components of how the raceway, or mounting, vibrates in time [35, 38, 44]. Current methods perform best for identifying localised defects that create an impulsive response; given the right conditions these methods can identify whether there is a localised defect on the inner or outer race, or on the rollers themselves. However, it has been challenging to make current methods robust and reliable

¹Corresponding author: arturgower@gmail.com

enough to automate, and therefore experts are often required to both process and interpret the results.

Too few sensors. It is likely that robust diagnostics are not possible for a small number of sensors. Typically, sensors measure displacement or acceleration at one or two positions, and rotation speed on each large bearing [24]. That is, there are often too many unknowns for the number of sensors typically used. Further, acceleration sensors are often placed on the housing, in which case the *transfer path* of the signal can be unknown and complex. We call the *transfer path* the route an elastic wave takes from its source to a sensor.

Be more quantitative. In this work we suggest that to have more robust and automatic predictions we need to properly model the physics of elastic waves in the bearing raceway. After all, these elastic waves are what carry the information of the forces inside the bearing to the sensors. Modelling elastic waves enable us to: 1) determine how well we can truly expect a few sensors to perform, and 2) develop more quantitative methods to predict defects and contact forces in bearings.

A typical approach to account for the physics of elastic waves is to use finite element methods, however these are far too computationally intensive and opaque for inverse problems [43]. In this paper we show how elastic waves can be very efficiently described both for sensing and modelling, with details in the next section.

Nonlinear dynamics at interfaces. For roller and journal bearings the way that forces are transmitted through the bearing and the shaft at interfaces are non-linear [6, 18, 41]. For example, a roller rattling is a non-linear dynamic event. Non-linearities at the interfaces make it challenging to accurately solve for the dynamics of an entire system, which typically includes components like shafts, rotors, bearings, and varying foundations [23]. Over the past 40 years there has been significant work to model the entire system [24, 31, 32, 33, 42].

Linear elastic waves. While the interface conditions between machine components are often non-linear, the elastic waves within each component are primarily governed by linear elasticity. This allows us to break the problem into manageable parts: by measuring the vibrations at one boundary, we can predict the forces or vibrations at another boundary of the same component.

We demonstrate that it is possible to accurately predict the stresses on a bearing raceway. See Figure 1 for a motivational example which predicts the stresses between the rollers and the raceway with just four sensors. There is currently no such method to predict the forces in a bearing which are important for lifetime analysis and to understand the causes of defects [15].

Acoustic emission and localisation. One way to diagnose when defects appear is to measure the sound a defect emits when it forms or expands [8, 19, 20]. These methods rely on measuring only pressure waves in solid components and are almost exclusively based in the time domain, where the first signal that arrives is (likely) the bulk pressure mode. It is important to only use the first measured signal, as the next signals will be a mix of acoustic and shear waves that have likely mode converted at boundaries, and, especially for thin structures, potentially formed waveguide modes. To extract the first signal can be difficult when its amplitude is far less than the other wave modes, and, of course, its arrival time is

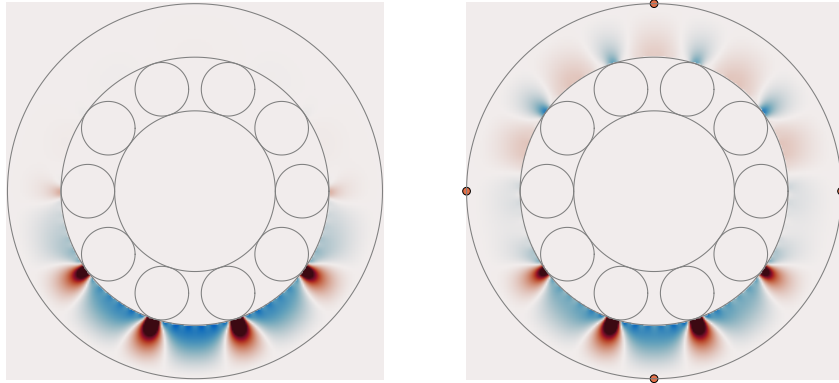


Figure 1: True pressure on the left for one snapshot in time. The right shows the predicted stress for the same time when using 4 sensors shown as orange spots. The sensors measure displacement, and the outer boundary is stress free, which is why the stress tends to zero when it reaches the outer boundary. However, the displacements or accelerations caused by the stress are not zero on this boundary and can be measured. The recovery is not perfect as there is a 20% error added to the boundary data. More details given in Section 7.3.

unknown. [12]

Alternatively, instead of assuming that there are only acoustics waves, one could just measure the signal in time, potentially both pressure and shear displacement, and from that determine where the source is. To do so would require modelling elastic waves. This paper is the first step to an elastic emission method in bearing raceways that does not require extracting the first arrival time, and could continually measure and identify sources.

Paper contents. In this paper we show theoretical and numerical results on how to predict the stress on the raceway and between rollers and the raceway. The methods developed can be specialised to other bearings, though we focus on roller bearings here.

In Section 2 we discuss how, at high enough frequencies, elastic waves are mostly confined to the bearing raceway; this allows us to model the waves in a raceway as vibrations of a hollow cylinder, as opposed to modelling the full bearing system. In Section 3 we develop a modal method and show how to use boundary conditions to quickly calculate elastic waves in the raceway.

In Section 4 we show how assumptions about the boundary conditions, which we call priors, can greatly reduce the number of sensors required. As an example, in Section 5 we show how to deduce and use priors about rollers rotating at a constant speed.

From the elastic wave models we learn what is, and is not, measurable, which we summarise in Section 6. In Section 7 we show several numerical examples both for validation and to illustrate the main results.

2 Elastic waves in raceways

Bearings are mounted in many different ways, one example is shown in Figure 2. However, the raceway is usually a hollow cylinder and is fabricated as one solid piece, see Figure 3 for some examples. The raceway is then tightly fitted into the mounting, or if there is also an inner raceway then it is fitted over a shaft.

When the rollers press on the track, they emit elastic waves, which for high enough frequencies ($> 10\text{kHz}$ s) are mostly trapped within the track [36] due to the air gap that remains between the raceway and the mounting (or shaft). However, for convenience, sensors are usually placed on the bearing mounting, rather than the raceway itself, which does not always get a good signal for bearing defects, or other features. In many cases, the waves originally emitted into the raceway can take a long (transmission) path until reaching a sensor on the mounting. During this journey, the wave is highly distorted; this can make it difficult to recognize defects signals [40]. There are methods which attempt to undo the effects of this path [35] for impulsive signals, e.g. minimum entropy deconvolution [40]. However, these can not be generalised to non impulsive signals; can enhance noise that is impulsive and have some difficulties in parameter choice such as window length [4].

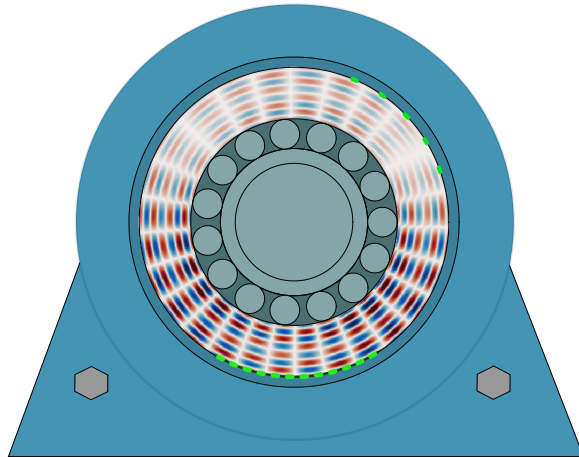


Figure 2: A cross section illustration of a bearing in a mounting. Showing a wave for a fixed frequency ($> 10\text{kHz}$ s) showing waves trapped in the raceway. Further shown are sensors mounted on the raceway as we propose.

What if we could mount sensors on, or near, a part of the raceway, as shown in Figure 2? This has added complications as it needs to be planned into the design of the bearings, but, as show in this paper, it would also lead to many benefits such as a direct prediction of the stresses in bearings, and clear signals on defects, be them extended or localised. We can answer exactly what is possible to predict; what frequencies to use and where to place the sensors just considering that the raceway is approximately a hollow cylinder, as we do in the next section.



Figure 3: The left shows a Schaeffler roller bearing for the main shaft of a wind turbine [39] while the right shows an example of a Miba tilting pad journal bearing used in turbines[3]. In both examples sensors could be placed on the outside of the casing before putting the bearing in its mounting.

2.1 Modal solution

Below we show the simplest way to calculate elastic waves in the raceway, see Figure 4 for an illustration of the boundaries and domain where we calculate elastic waves.

Steel is well approximated as an isotropic material. Further, as even very high stresses of 1000 MPa only change elastic wave speeds by a few percent [25], the elastic waves within the raceway are well approximated by the linearised equations of elasticity in a homogeneous and isotropic solid [27]. We also assume that stresses applied to the raceway boundaries are approximately axially symmetric, at least after averaging over some time period, which implies that the elastic waves are axially symmetric.

The above allows us to write the small elastic displacement, for a harmonic angular frequency of ω in terms of the Helmholtz potentials in the form

$$\mathbf{u} = \nabla\phi + \nabla \times (\psi\hat{\mathbf{z}}) \quad (2.1)$$

where ϕ and ψ are the pressure and shear potentials respectively, and noting that the vector shear potential automatically satisfies the divergence free condition $\nabla \cdot (\psi\hat{\mathbf{z}}) = 0$ when ψ does not depend on z . The displacement in time can be easily calculated by taking an inverse Fourier transform, which is the same as integrating $\mathbf{u}e^{-i\omega t}$ over ω in the convention used here.

The advantage of using the Helmholtz decomposition (2.1) is that both potentials satisfy a Helmholtz equation:

$$\nabla^2\phi + k_p^2\phi = 0, \quad \nabla^2\psi + k_s^2\psi = 0, \quad (2.2)$$

where $k_p = \frac{\omega}{c_p}$ and $k_s = \frac{\omega}{c_s}$ are the wavenumbers of the P and S-waves, while c_p and c_s are the wave speeds which are related to the Lamé parameters λ and μ through

$$\rho c_p^2 = \lambda + 2\mu \quad \text{and} \quad \rho c_s^2 = \mu, \quad (2.3)$$

where ρ is the mass density.

As we consider the raceway to be a thick-walled circular cylinder, we can reach simple solutions by using cylindrical coordinates (r, θ) , which leads to solutions of (2.2) in the form

$$\begin{aligned}\phi(r, \theta) &= \sum_{n=-\infty}^{\infty} \left(a_n J_n(k_p r) + b_n H_n^{(1)}(k_p r) \right) e^{in\theta}, \\ \psi(r, \theta) &= \sum_{n=-\infty}^{\infty} \left(c_n J_n(k_s r) + d_n H_n^{(1)}(k_s r) \right) e^{in\theta},\end{aligned}\tag{2.4}$$

where J_n and $H_n^{(1)}$ are Bessel and Hankel functions of the first kind respectively. To deduce above you can use separation of variables [2, 28], and the coefficients a_n, b_n, c_n, d_n can be determined from boundary conditions. Note that if the cylinder had no hole, then $b_n = d_n = 0$ and there would also be one less boundary to prescribe boundary conditions.

To prescribe boundary conditions we need the traction on the boundary in polar coordinates. In general the Cauchy stress tensor is given by

$$\boldsymbol{\sigma} = \lambda \text{tr}(\boldsymbol{\varepsilon}) \mathbf{I} + 2\mu \boldsymbol{\varepsilon}\tag{2.5}$$

where $\boldsymbol{\varepsilon} = \frac{1}{2} (\nabla \mathbf{u} + \nabla \mathbf{u}^T)$. The traction $\boldsymbol{\tau}$ on the outer boundary of a cylinder is given by

$$\boldsymbol{\tau} = \boldsymbol{\sigma} \cdot \hat{\mathbf{r}} = \sigma_{rr} \hat{\mathbf{r}} + \sigma_{r\theta} \hat{\boldsymbol{\theta}},\tag{2.6}$$

where $\hat{\mathbf{r}}$ and $\hat{\boldsymbol{\theta}}$ are unit vectors along the directions that the radius and polar angle increase. The traction on the inner boundary is given by $\boldsymbol{\tau} = -\boldsymbol{\sigma} \cdot \hat{\mathbf{r}}$ as the outward normal vector in this case is $-\hat{\mathbf{r}}$. See [9] for more details on stress tensors in polar coordinates.

Substituting (2.1) into (2.5) leads to

$$\sigma_{rr} = (2c_s^2 k_p^2 - \omega^2) \rho \phi + 2\rho c_s^2 \left[\frac{\partial^2 \phi}{\partial r^2} + \frac{\partial}{\partial r} \left(\frac{1}{r} \frac{\partial \psi}{\partial \theta} \right) \right],\tag{2.7}$$

$$\sigma_{r\theta} = -\rho \omega^2 \psi - 2\rho c_s^2 \left[\frac{\partial^2 \psi}{\partial r^2} - \frac{\partial}{\partial r} \left(\frac{1}{r} \frac{\partial \phi}{\partial \theta} \right) \right].\tag{2.8}$$

See Appendix B for derivation.

3 Boundary conditions

How much boundary data is needed to determine the potentials in Equation (2.4)? To answer this question, consider the simpler case of how much data is needed to determine just the coefficients a_n in a series $f(\theta) = \sum_n a_n e^{in\theta}$; representing any square integrable periodic function $f(\theta)$ (almost everywhere). To determine a_n we need to supply a function $f(\theta)$. Therefore, to determine $a_n, b_n, c_n,$ and d_n we must supply four functions.

For example, let us turn to Figure 4 and consider the outer raceway. To determine all the coefficients, it would be sufficient to have the boundary data of the displacement \mathbf{u} and traction $\boldsymbol{\tau}$ on just one boundary, say at $r = r_1$, because

$$\mathbf{u}(r_1, \theta) = u_r(r_1, \theta) \hat{\mathbf{r}} + u_\theta(r_1, \theta) \hat{\boldsymbol{\theta}},$$

which is composed of two scalar functions in θ , and likewise for $\boldsymbol{\tau}$. If the source of the elastic waves was also on the boundary $r = r_1$, then this would be an initial value problem, and we expect it then to be well-posed, and therefore this boundary data would completely determine the coefficients.

Below we consider different combinations of boundary data and show how to determine the coefficients a_n , b_n , c_n , and d_n . In this work we do not discuss uniqueness of the solution, and simply verify that the solution is indeed well-posed where we expect it to be. That is, we expect the solution to become ill posed for low enough frequencies, and to be ill posed when approaching the diffraction limit, see Appendix C for details.

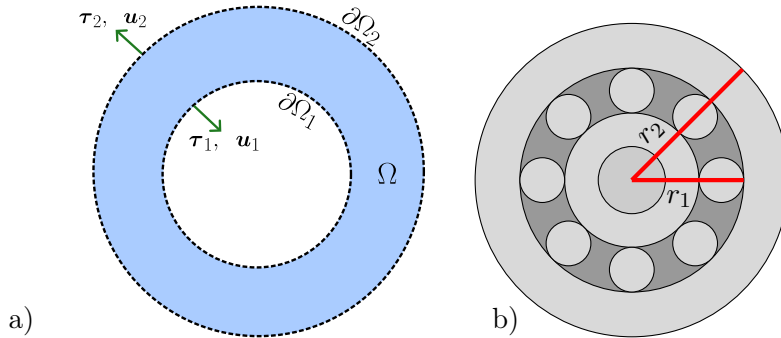


Figure 4: Image a) on the left shows the general boundary conditions we consider. That is, we describe elastic waves in the domain Ω , and will use some combination of the boundary data \mathbf{u}_1 , \mathbf{u}_2 , $\boldsymbol{\tau}_1$, $\boldsymbol{\tau}_2$ on the boundaries $\partial\Omega_1$ and $\partial\Omega_2$ which are defined by $r = r_1$ and $r = r_2$ respectively. The image b) on the right illustrates the geometry of one type of roller bearing, where the radii of the outer raceway are shown as an example. The methods of this paper could be used to predict the stresses between either the rollers and outer raceway or the rollers and the inner raceway.

We call the *forward problem* the case where the traction $\boldsymbol{\tau}$ on the inside and outside of the raceway are given. The name is just for convenience, and because knowing the traction on both boundaries often implies we know the source of the waves. However, this is still a boundary value, and could equally be considered to be an inverse problem. We consider this case first and then turn to more general boundary conditions, such as the case where the displacement \mathbf{u} and traction $\boldsymbol{\tau}$ on the outer boundary are known, which we call the *inverse problem*. Finally, we look at some example with stresses inspired by an operating bearing.

The inverse problem is of more practical importance, as it is possible to place sensors on the outside of the raceway for the case shown in Figure 4. In Section 3.3 we discuss the details on taking boundary data from a, possibly small, finite number of measurements at specific points on the boundary.

3.1 Traction boundary conditions: the forward problem

Here we consider prescribing only traction boundary conditions on both the boundaries of the raceway, see Figure 4 for an illustration.

Let the traction on the boundary $r = r_1$ be $\boldsymbol{\tau}^1(\theta)$, and the traction on the boundary $r = r_2$ be $\boldsymbol{\tau}^2(\theta)$, be given by;

$$\boldsymbol{\tau}^1(\theta) = -p^1(\theta)\hat{\mathbf{r}} - s^1(\theta)\hat{\boldsymbol{\theta}}, \quad \boldsymbol{\tau}^2(\theta) = p^2(\theta)\hat{\mathbf{r}} + s^2(\theta)\hat{\boldsymbol{\theta}}, \quad (3.1)$$

where the negative sign in the top equation is due to the unit normal being $-\hat{\mathbf{r}}$.

To solve the problem now we need the Fourier series representation:

$$p^j(\theta) = \sum_{n=-\infty}^{\infty} p_n^j e^{in\theta}, \quad s^j(\theta) = \sum_{n=-\infty}^{\infty} s_n^j e^{in\theta}, \quad \text{for } j = 1, 2, \quad (3.2)$$

then substitute the potentials (2.4) into (2.7) and (2.8) and then substitute the result into (3.1). Using that the $e^{in\theta}$ in the Fourier series are orthonormal leads to the matrix equation

$$\mathbf{M}_n^{\text{for}} \mathbf{a}_n = \mathbf{f}_n, \quad (3.3)$$

for the mode n ; where,

$$\mathbf{a}_n = [a_n, b_n, c_n, d_n]^T \quad \text{and} \quad \mathbf{f}_n = [p_n^1, s_n^1, p_n^2, s_n^2]^T.$$

The expressions for the components of the 4×4 matrix $\mathbf{M}_n^{\text{for}}$ involve known special functions and can be found in Appendix A. If the matrix is well conditioned, then we can solve (3.3) for the coefficients \mathbf{a}_n . In practice, we numerically check whether $\mathbf{M}_n^{\text{for}}$ is well conditioned for $n = 0$, and then increase $|n| = 1, 2, \dots$ until $\mathbf{M}_n^{\text{for}}$ is not well conditioned. Further details on when this problem is ill-posed can be found in Section 6 and Appendix C.

3.2 Data on only one boundary: the inverse problem

In practice it is not possible to know the traction on both boundaries. For example in the image on the right of Figure 4 it is clearly not feasible to have sensors on the boundary $r = r_1$, however the boundary $r = r_2$ is often approximately traction free, due to the small air gap between the raceway and mounting. If we place ultrasonic sensors on the boundary $r = r_2$ then we would also know the displacement \mathbf{u}_2 . See Figure 12 for an illustration. In the next section we discuss how to deal with a finite number of sensors, but for the remainder of this section we consider that both the traction and displacement are known on the boundary $r = r_2$.

Analogous to the previous section, we write the displacement on the outer-boundary as a Fourier series

$$\mathbf{u}(r_2, \theta) = \mathbf{u}^2(\theta) = \sum_n u_n^{(r)} \hat{\mathbf{r}} e^{in\theta} + \sum_n u_n^{(\theta)} \hat{\boldsymbol{\theta}} e^{in\theta},$$

then by substituting the potentials (2.8) (2.7) into the expression for \mathbf{u} in (2.1), and then substituting the result into the above leads to two separate equations. Combining these two equations with the two equations for the traction boundary data $\boldsymbol{\tau}^2$ from the previous section, and again using that the modes of the Fourier series are orthogonal leads to another 4×4 matrix equation:

$$\mathbf{M}_n^{\text{inv}} \mathbf{a}_n = \mathbf{u}_n. \quad (3.4)$$

If $\mathbf{M}_n^{\text{inv}}$ is well conditioned, then we can solve for \mathbf{a}_n , and this solution will also solve the forward problem (3.3). An example of solving a transient point force is given in Section 7.1

3.3 Measured points on the boundary

Let us start by summarising our results so far. In Section 3 we showed how to form a system

$$\mathbf{M}_n \mathbf{a}_n = \mathbf{f}_n, \quad (3.5)$$

for some given choice of boundary conditions, where the vector \mathbf{f}_n contains the Fourier modes from measurements on the boundaries, i.e. the measured displacement and/or traction, and \mathbf{M}_n is a known 4-by-4 matrix that depends on the type of boundary conditions. In practice, we do not have direct access to the Fourier modes of the boundary data \mathbf{f}_n , but instead measure the elastic wave displacement at specific points on the boundary. That is, by summing up the Fourier modes on both sides of the modal system (3.5) we obtain:

$$\sum_n e^{in\theta} \mathbf{M}_n \mathbf{a}_n = \sum_n e^{in\theta} \mathbf{f}_n, \quad (3.6)$$

where $\mathbf{y}(\theta) := \sum_n e^{in\theta} \mathbf{f}_n$ represents all the boundary data as a function of θ . In practice we may measure $\mathbf{y}(\theta)$ at specific angles θ and from this want to obtain the \mathbf{a}_n .

A sophisticated approach would consider that $\mathbf{y}(\theta)$ is some statistical distribution that is estimated from measured data. However, in this work we want to keep the presentation as simple as possible. So instead, we show how to rewrite the system (3.6) in terms of a finite number of deterministic measurements on the boundaries.

First note that $\mathbf{y}(\theta)$ covers two different boundaries, each of which could be sampled at different angles θ . To accommodate this we rewrite (3.6) sampled at discrete angles

$$\sum_n \begin{bmatrix} e^{in\theta_{m_1}^1} \mathbf{M}_n^1 \\ e^{in\theta_{m_2}^2} \mathbf{M}_n^2 \end{bmatrix} \mathbf{a}_n = \begin{bmatrix} \mathbf{y}_{\text{inv}}^1(\theta_{m_1}^1) \\ \mathbf{y}_{\text{inv}}^2(\theta_{m_2}^2) \end{bmatrix}, \quad (3.7)$$

where we evaluate $m_1 = 1, 2, \dots, M_1$ to iterate over the M_1 measured points $\theta_1^1, \theta_2^1, \dots, \theta_{M_1}^1$. Likewise, we evaluate $m_2 = 1, 2, \dots, M_2$. However, to facilitate implementation, we want to iterate over just one index m , rather than m_1 and m_2 , which leads us to rewrite the left of (3.7) in the form

$$\sum_n \mathbf{E}_{mn} \mathbf{a}_n = \begin{bmatrix} \chi_m^1 \mathbf{y}_{\text{inv}}^1(\theta_m^1) \\ \chi_m^2 \mathbf{y}_{\text{inv}}^2(\theta_m^2) \end{bmatrix} \quad \text{with} \quad \mathbf{E}_{mn} := \begin{bmatrix} \chi_m^1 e^{in\theta_m^1} \mathbf{M}_n^1 \\ \chi_m^2 e^{in\theta_m^2} \mathbf{M}_n^2 \end{bmatrix}, \quad (3.8)$$

where $\chi_m^1 = 1$ if $1 \leq m \leq M_1$, and otherwise $\chi_m^1 = 0$, and χ_m^2 has the analogous definition. We note the technicality that θ_m^j is not defined if $\chi_m^j = 0$, which we can remedy by setting $\theta_m^j = 0$ when $\chi_m^j = 0$.

To solve (3.8) it is best to rewrite it in the block matrix form:

$$\mathbf{E}\mathbf{a} = \mathbf{y}, \quad (3.9)$$

where \mathbf{E} is a block matrix with the matrix block components \mathbf{E}_{mn} , \mathbf{a} is a block vector from vertically stacking the vectors \mathbf{a}_n , and likewise \mathbf{y} is a block vector which results from vertically stacking the vectors on the right side of (3.8).

Finally, for (3.9) to have a unique solution for \mathbf{a} then the number of modes N considered for \mathbf{a}_n has to satisfy $N \leq M_1$ and $N \leq M_2$.

4 Priors and recovering the load from the rollers

The methods shown in Section 3 make no assumptions about the boundary conditions. If we make no assumptions about the internal geometry, or sources of the elastic waves, then we may need a lot of sensors to obtain detailed prediction of the boundary data, as shown in Section 7.2. To use a small number of sensors we need to provide some information, which we call priors.

For example, using a tachometer (a revolution counter), together with the design specifications of the roller bearing, we would know approximately the speed of the rollers and their contact points. We show later that this in itself is a powerful prior.

4.1 Linear priors

Any prior information about the source of waves, such as a known number of roller bearings, will allow us to parameterise \mathbf{a} in some way. For instance, a linear parameterisation:

$$\mathbf{a} = \mathbf{B}\mathbf{x} + \mathbf{c}, \quad (4.1)$$

where the matrix \mathbf{B} , and bias vector \mathbf{c} , are known from the prior information, while \mathbf{x} is now the unknown. We assume that \mathbf{B} is full-column rank. For the above to be a restriction on \mathbf{a} the matrix \mathbf{B} has to have more rows than columns. We will show later how a linear relationship between \mathbf{a} and \mathbf{x} covers many important cases.

Substituting (4.1) into the block modal equation (3.9) then leads to

$$\mathbf{E}\mathbf{B}\mathbf{x} + \mathbf{E}\mathbf{c} = \mathbf{y}, \quad (4.2)$$

where we use a pseudo inverse to obtain a solution

$$\mathbf{x}_\star = (\mathbf{E}\mathbf{B})^+(\mathbf{y} - \mathbf{E}\mathbf{c}). \quad (4.3)$$

For the above to give a unique solution, we have also assumed that \mathbf{E} is full rank. Substituting the above into (4.1) leads to

$$\mathbf{a}_\star = \mathbf{B}(\mathbf{E}\mathbf{B})^+(\mathbf{y} - \mathbf{E}\mathbf{c}) + \mathbf{c}. \quad (4.4)$$

The solution \mathbf{a}_\star would be equal to \mathbf{a} when \mathbf{EB} is a square matrix, otherwise \mathbf{a}_\star is a least squares approximation to \mathbf{a} . We give an example for roller bearings in Section 7.3.

Note that while the inverse of \mathbf{E} could be ill defined, the pseudo inverse of \mathbf{EB} could be well defined, as we expect the dimension of \mathbf{x} to be much smaller than the dimension of \mathbf{a} .

4.2 Prior due to boundary conditions

One of the most general ways to have a linear prior, as shown in Section 4.1, is to have a linear basis for the boundary conditions. For example, the boundary where the rollers make contact with the raceway leads to a basis as shown in Section 5.

In this section we use $\mathbf{M}_n^{\text{for}}$ and \mathbf{E}^{for} to represent the modal matrix and block matrix in (3.5) and (3.9) for the boundary conditions for which we have prior knowledge. The "for" in \mathbf{M}^{for} stands for forward problem¹. We use $\mathbf{M}_n^{\text{inv}}$ and \mathbf{E}^{inv} for problems which are ill posed, where "inv" represents inverse problem.

To completely determine the elastic waves within the bearing would require the boundary data $\mathbf{y}_{\text{for}}^1(\theta)$ and $\mathbf{y}_{\text{for}}^2(\theta)$, each of which can be written in terms of scalar functions in the form

$$\mathbf{y}_{\text{for}}^1(\theta) = \begin{bmatrix} p^1(\theta) \\ s^1(\theta) \end{bmatrix} \quad \text{and} \quad \mathbf{y}_{\text{for}}^2(\theta) = \begin{bmatrix} p^2(\theta) \\ s^2(\theta) \end{bmatrix}. \quad (4.5)$$

For example, if the boundary data $\mathbf{y}_{\text{for}}^1(\theta)$ represents the traction (see Figure 4), then $p^1(\theta)$ and $s^1(\theta)$ would represent the pressure and shear force as a function of the angle θ .

To reach a linear prior (4.1), we assume there is a known basis for the boundary data:

$$\mathbf{y}_{\text{for}}^1(\theta) = \sum_{\ell=0}^{L_1} x_\ell^1 \mathbf{y}_\ell^1(\theta) + \mathbf{b}^1(\theta), \quad \mathbf{y}_{\text{for}}^2(\theta) = \sum_{\ell=0}^{L_2} x_\ell^2 \mathbf{y}_\ell^2(\theta) + \mathbf{b}^2(\theta), \quad (4.6)$$

where the $\mathbf{y}_\ell^j(\theta)$ and $\mathbf{b}^j(\theta)$ are known, and the x_ℓ^j are, for now, unknown. Each of these functions can be decomposed in Fourier modes:

$$\mathbf{y}_\ell^j(\theta) = \sum_n \mathbf{f}_{\ell n}^j e^{in\theta} \quad \text{and} \quad \mathbf{b}^j(\theta) = \sum_n \mathbf{b}_n^j e^{in\theta}, \quad \text{for } j = 1, 2. \quad (4.7)$$

Using the above, we can write the boundary conditions for one mode in the form:

$$\mathbf{M}_n^{\text{for}} \mathbf{a}_n = \begin{bmatrix} \mathbf{F}_n^1 \mathbf{x}^1 \\ \mathbf{F}_n^2 \mathbf{x}^2 \end{bmatrix} + \begin{bmatrix} \mathbf{b}_n^1 \\ \mathbf{b}_n^2 \end{bmatrix}, \quad (4.8)$$

where we define

$$\mathbf{F}_n^j = \begin{bmatrix} \mathbf{f}_{1n}^j & \mathbf{f}_{2n}^j & \cdots & \mathbf{f}_{L_j n}^j \end{bmatrix}, \quad (4.9)$$

¹Although it is debatable what is a forward or inverse problem here.

so that $\mathbf{F}_n^j \mathbf{x}^j = \sum_{\ell} \mathbf{f}_{\ell n}^j x_{\ell}^j$. To write the above in a block matrix form we define

$$\mathbf{b}_n = \begin{bmatrix} \mathbf{b}_n^1 \\ \mathbf{b}_n^2 \end{bmatrix}, \quad \mathbf{x} = \begin{bmatrix} \mathbf{x}^1 \\ \mathbf{x}^2 \end{bmatrix}, \quad \text{and} \quad \mathbf{F}_n = \begin{bmatrix} \mathbf{F}_n^1 & 0 \\ 0 & \mathbf{F}_n^2 \end{bmatrix}, \quad \text{so that} \quad \mathbf{F}_n \mathbf{x} = \begin{bmatrix} \mathbf{F}_n^1 \mathbf{x}^1 \\ \mathbf{F}_n^2 \mathbf{x}^2 \end{bmatrix}, \quad (4.10)$$

and then rewrite (4.8) in a block form to obtain

$$\mathbf{M}^{\text{for}} \mathbf{a} = \mathbf{F}^{\text{for}} \mathbf{x} + \mathbf{b}^{\text{for}}, \quad \text{with} \quad \mathbf{F}^{\text{for}} = \begin{bmatrix} \vdots \\ \mathbf{F}_{-1} \\ \mathbf{F}_0 \\ \mathbf{F}_1 \\ \vdots \end{bmatrix} \quad \text{and} \quad \mathbf{b}^{\text{for}} = \begin{bmatrix} \vdots \\ \mathbf{b}_{-1} \\ \mathbf{b}_0 \\ \mathbf{b}_1 \\ \vdots \end{bmatrix}, \quad (4.11)$$

where \mathbf{M}^{for} is a block diagonal matrix with $\mathbf{M}_n^{\text{for}}$ on the diagonals, and we have added the superscript “for” to emphasize that these above quantities are related to the forward problem. Note that if we knew the boundary data of the forward problem we would have $\mathbf{f}^{\text{for}} = \mathbf{F}^{\text{for}} \mathbf{x} + \mathbf{b}^{\text{for}}$.

Finally, we take the inverse of \mathbf{M}^{for} on both sides of (4.11) to obtain

$$\mathbf{a} = (\mathbf{M}^{\text{for}})^{-1} \mathbf{F}^{\text{for}} \mathbf{x} + (\mathbf{M}^{\text{for}})^{-1} \mathbf{b}^{\text{for}}, \quad (4.12)$$

where we have assumed that the type of boundary conditions that lead to \mathbf{M}^{for} lead to a well conditioned problem so that calculating the inverse $(\mathbf{M}^{\text{for}})^{-1}$ is stable and well defined.

The restriction (4.12) on \mathbf{a} now matches the abstract form given by (4.15), where by comparison we obtain:

$$\mathbf{B}^{\text{for}} = (\mathbf{M}^{\text{for}})^{-1} \mathbf{F}^{\text{for}} \quad \text{and} \quad \mathbf{c}^{\text{for}} = (\mathbf{M}^{\text{for}})^{-1} \mathbf{b}^{\text{for}}. \quad (4.13)$$

We can use the above restriction to solve for \mathbf{a} even when given incomplete boundary data. Let us write this out in full for clarity.

Let $\mathbf{E} = \mathbf{E}^{\text{inv}}$ and $\mathbf{y} = \mathbf{y}^{\text{inv}}$ in (3.9) to indicate that calculating $(\mathbf{E}^{\text{inv}})^{-1}$ is either ill-posed or that the measured \mathbf{y}^{inv} is incomplete boundary data. Our aim is now to solve

$$\mathbf{E}^{\text{inv}} \mathbf{a} = \mathbf{y}^{\text{inv}}. \quad (4.14)$$

Using the result (4.4) together with the substitutions (4.13) leads to the solution

$$\mathbf{a}_{\star} = \mathbf{B}^{\text{for}} (\mathbf{E}^{\text{inv}} \mathbf{B}^{\text{for}})^+ (\mathbf{y}^{\text{inv}} - \mathbf{E}^{\text{inv}} \mathbf{c}^{\text{for}}) + \mathbf{c}^{\text{for}}. \quad (4.15)$$

It is likely easier to understand this result, and its consequences, with a concrete example which we provide for roller bearings in Section 5. Nonetheless, let us consider some here important features of this solution.

To simplify the discussion here, let us assume that the number of boundary measurements \mathbf{y}^{inv} is equal to the number of unknowns in \mathbf{x} so that $\mathbf{a}_{\star} = \mathbf{a}$ and $\mathbf{E}^{\text{inv}} \mathbf{B}^{\text{for}}$ is a square matrix. So if we have a representation for \mathbf{a} that uses a small number of basis elements L_1 and L_2

in (4.6), then we need only a small number of measurements in \mathbf{y}^{inv} to obtain the unique solution \mathbf{a} . In Section 5 we show how assuming a smooth loading of a roller bearing leads to small values for L_1 and L_2 . To further emphasize this point, note that the resolution of the solution is governed by the number of modes N in \mathbf{a} . That is, the block vector \mathbf{a} is formed of the vectors \mathbf{a}_n with n having N possible values. For a fixed number of basis' L_1 and L_2 in (4.6) we can increase N and still obtain the unique solution \mathbf{a} as long as \mathbf{M}^{for} in (4.12) continues to be well conditioned. This is why the images in Figure 1 have such high resolution, despite having only 3 sensors.

4.3 One traction free boundary

Here we give an example which is typical for bearings: the traction on one boundary is known, and the boundary in contact with the roller bearings has a basis function. For example the outside boundary in Figure 4 could be traction free.

For this case, we need to make a small adjustment to the prior method shown in the previous section. Here the boundary data is of the form

$$\mathbf{y}_{\text{for}}^1(\theta) = \sum_{\ell=0}^{L_1} x_{\ell}^1 \mathbf{y}_{\ell}^1(\theta), \quad \mathbf{y}_{\text{for}}^2(\theta) = \mathbf{b}^2, \quad (4.16)$$

so that $\mathbf{b}^1(\theta) = \mathbf{0}$ and $\mathbf{x}^2 = \mathbf{0}$.

Following the same steps shown in the previous section, we would need to make a small adjustment by redefining

$$\mathbf{x} = \mathbf{x}^1, \quad \text{and} \quad \mathbf{F}_n = \begin{bmatrix} \mathbf{F}_n^1 \\ 0 \end{bmatrix}. \quad (4.17)$$

5 Roller bearings and the loading profile

Here we develop an application for roller bearings that shows the great potential of describing the elastic waves in the raceway in more detail.

Consider a roller bearing as shown on the left of Figure 3 and on the right of Figure 4. Any load applied to the shaft in the middle of the bearing, or applied to the outer raceway, will be transmitted through the rollers themselves with each roller in contact with only a small region of the raceway, as illustrated in Figure 5. We do not need to know the exact shape of this small contact region if the goal is just to measure the overall load passed through the bearing; as long as the contact region is small compared to the bearing geometry. Below we show how knowing the rotation speed of the bearing, number of bearings, and their contact points, can lead us to predict the load transmitted through each bearing with very few sensors.

We make a number of simplifying assumptions, which can improved on in future work. First, in practice, rollers slip as they go around [35], making their contact points better described as a random variable. Further, the contact points of the bearings with the raceway are more accurately modelled as Hertzian contacts [5]. However, here we show only how

to use deterministic priors both for simplicity but because it is necessary to develop the deterministic version first before developing more precise models with random variables. Second, we assume the bearing is rotating at a constant speed Ω . The framework we present can accommodate any change in rotation speed, but the conclusions shown below would need to be adjusted.

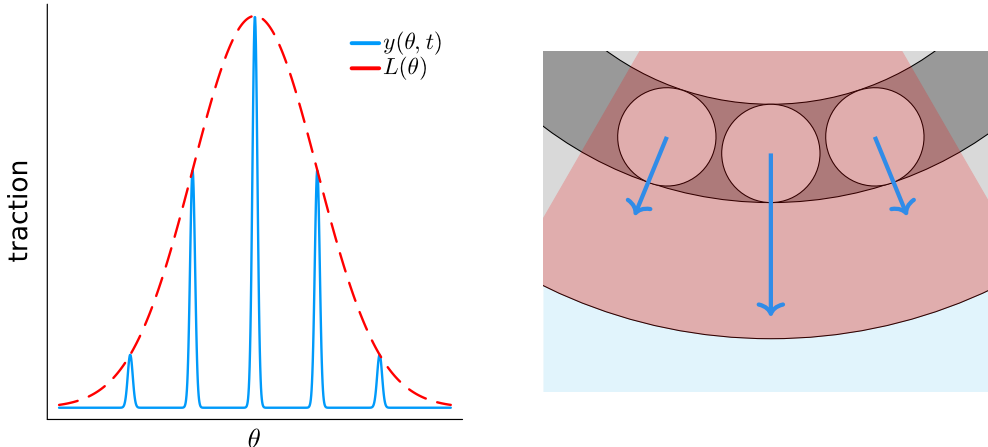


Figure 5: The graph on the left shows the stress on the raceway boundary $y(\theta, t)$. Each blue spike is the result of one roller being in contact with the raceway. As the rollers move in time, the blue spikes in this graph also move, but they all trace the same curve $L(\theta)$, where we assume the load supported by the bearing does not change in time. The image on the right illustrates how load is transmitted through the rollers.

5.1 Static Loading profile

Imagine the bearings are loaded just due to gravity, or some other static forces on the shaft, mounting, or casing. We use the function $L(\theta)$ to denote the stress transmitted through a roller when it is in contact with the raceway at an angle θ . We call $L(\theta)$ the loading profile and in this section assume it is independent of time. So this excludes environment effects, for example.

Assume that $L(\theta)$ represents the radial stress for simplicity, and that the contact region of the roller is small, then we can write that the radial stress on the boundary $y(\theta, t)$ of the raceway is given by

$$y(\theta, t) = L(\theta)d(\theta, t), \quad \text{where} \quad d(\theta, t) = \sum_{s=-\infty}^{\infty} \delta((\theta - \Omega t)Z + 2\pi s), \quad (5.1)$$

where Z is the number of roller bearings, Ω their angular speed, t is time, and the function $\delta(\theta)$ represents the stress distribution due to one roller. See Figure 5 for an illustration. A form similar to (5.1) for the stress on the boundary was introduced in [31] and [32].

The function $d(\theta, t)$ moves the contact points of the bearing as time passes, and assumes that the Z bearings have the same distance between each other. We assume that each $\delta((\theta - \Omega t)Z + 2\pi s)$ when integrated over θ is equal to 1, so that the magnitude of the load transmitted is always $L(\theta)$, no matter the shape of the function $\delta(\theta)$. We could, for example have the function δ be as scaled Dirac delta function. However to avoid Gibbs phenomena it is best to use a Gaussian function:

$$\delta(x) = \frac{Z}{\sigma} e^{-\pi x^2 / \sigma^2}, \quad (5.2)$$

where σ is the standard deviation of the contact spread. In the limit of $\sigma \rightarrow 0$ the above δ would become a scaled Dirac delta. Naturally, we could use other type of contact points, but when the aim is to measure $L(\theta)$ we do not need to model precisely the contact region.

The function $d(\theta, t)$ is periodic in time with period $T = 2\pi / (Z\Omega)$, which means we can write $d(\theta, t)$ in terms of its Fourier series in time, which (after some calculations) is given by

$$d(\theta, t) = \frac{Z}{2\pi} \sum_{m=-\infty}^{\infty} e^{-\pi\sigma^2 m^2} \cos(mZ[\theta - \Omega t]), \quad \text{where } \omega_m = mZ\Omega. \quad (5.3)$$

The loading profile $L(\theta)$ is also 2π periodic in θ , so we use a Fourier series representation:

$$L(\theta) = \sum_n c_n e^{in\theta}, \quad (5.4)$$

which substituted into (5.1) together with (5.3), and after some calculations, leads to

$$y(\theta, t) = \sum_{n,m} f_n(\omega_m) e^{in\theta} e^{-i\omega_m t}, \quad \text{with } f_n(\omega_m) = \frac{Z}{2\pi} c_{n-mZ} e^{-\pi\sigma^2 m^2}, \quad (5.5)$$

which matches the notation from the previous sections.

Using the above, together with the prior method shown in Section 4.2 and Section 4.3, we can recover the coefficients of the loading profile c_n by measuring the displacement on the boundary of the raceway that is traction free. To do so, we first identify the unknowns $x_\ell = c_\ell$, then the matrix \mathbf{F}_n^1 would be full of zero except for the column number $\ell = n - mZ$ which would be

$$\mathbf{f}_{\ell,n}^1 = \frac{Z}{2\pi} \begin{bmatrix} e^{-\pi\sigma_P^2 m^2} \\ \mu_S e^{-\pi\sigma_S^2 m^2} \end{bmatrix},$$

where we assume the contact force distribution for the pressure σ_P is potentially different than the contact force for the shear σ_S , and we also assume that if the pressure is known, then the shear is known as consequence.

In the examples section, we show that four different sensors are needed to recover the load accurately, in steel, if the loading profile is smooth, as shown in Section 7.3. This is because a smooth loading profile implies that the series (5.4) needs few terms to converge.

5.2 Quasi-Static Loading profile

The most general force due to the rollers bearings on the raceway is given by

$$y(\theta, t) = L(\theta, t)d(\theta, t), \quad (5.6)$$

instead of (5.6). By taking the Fourier transform of both sides and using (5.3) with convolution theorem we obtain

$$\hat{y}(\theta, \omega) = \frac{Z}{2\pi} \sum_m e^{-\pi\sigma^2 m^2} \left(\hat{L}(\theta, \omega - \omega_m) e^{imZ\theta} + \hat{L}(\theta, \omega + \omega_m) e^{-imZ\theta} \right), \quad (5.7)$$

where $\hat{y}(\theta, \omega)$ and $\hat{L}(\theta, \omega)$ are the Fourier transforms of $y(\theta, t)$ and $L(\theta, t)$ respectively.

The form (5.7) would not be a useful prior if we knew nothing about \hat{L} . However, there is a useful and practical assumption that the loading is quasi-static, i.e. does not change rapidly. The simplest scenario being that $\hat{L}(\theta, \omega) \approx 0$ for $|\omega| > Z\Omega$, in which case the sum in (5.7) reduces to just one value for m , leading to

$$\hat{y}(\theta, \omega) = \frac{Z}{2\pi} e^{-\pi\sigma^2 m^2} \left(\hat{L}(\theta, \omega - \omega_m) e^{imZ\theta} + \hat{L}(\theta, \omega + \omega_m) e^{-imZ\theta} \right), \quad (5.8)$$

where $m = \left\lfloor \frac{\omega}{Z\Omega} \right\rfloor$, with $\lfloor x \rfloor$ being equal to x rounded to the nearest integer.

Analogous to the previous section, we decompose \hat{y} and \hat{L} in their Fourier modes to obtain

$$f_n(\omega) = \frac{Z}{2\pi} e^{-\pi\sigma^2 m^2} c_{n-mZ}(\omega - \omega_m). \quad (5.9)$$

6 What is measurable

It is not always possible to robustly estimate the stresses between the rollers, or other elements with elastic waves. There are two main phenomena that cause this: 1) resonance and 2) the diffraction limit. Numerically, we observe a relationship between the stability of the inverse problem and the frequency ω . In particular, we find that the numerical stability of the inverse problem increases as we increase the frequency, see Figure 6. This relationship between numerical stability and frequency is a well-established phenomenon in inverse problems for Helmholtz equations with Cauchy boundary conditions [7, 16, 17]. In particular [16, 17] show that for problems such as ours, the numerical stability of the inverse problem increases with the wavenumber k .

When hitting a resonance, the field inside (2.4) the raceway varies significantly with small changes of the boundary data. This occurs for the forward problem and interferes in using the prior method. To determine this precisely, we can turn to the modal system (3.3) or (3.4) and check if the matrix \mathbf{M}_n is well conditioned, with one example shown in Figure 6.

Due to the diffraction limit [30], for any fixed frequency there is a limited amount of information, or resolution that can be extracted. The maximum spatial resolution that

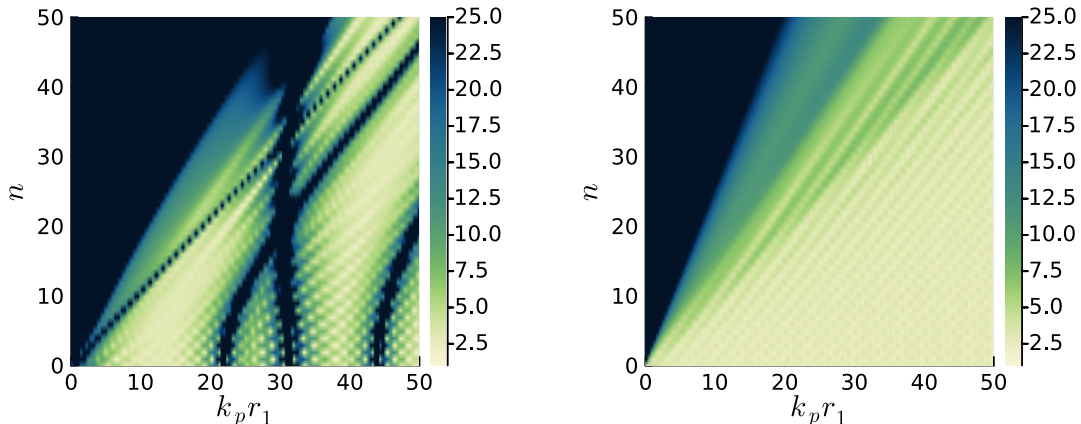


Figure 6: The above heatmaps show the condition number $\text{cond } \mathbf{M}_n^{\text{for}}$ on the left and $\text{cond } \mathbf{M}_n^{\text{inv}}$ on the right, after non-dimensionalisation. In the dark regions the errors in the boundary data can be amplified by 20 times. Note that for any fixed $k_p r_1$ if we keep increasing n the system will at some point become ill-conditioned. The dark cross and lines on the forward problem are resonant modes. The parameters used are given in Table 1.

can be recovered from the boundary is given by the largest mode number n used in the expansions (2.4). When fixing ω , the problem becomes more ill-posed as n grows larger.

The condition number of \mathbf{M}_n depends on the material parameters and geometry. In Appendix C we deduce an approximation to determine when the system is well posed, but this does not capture all the details shown in Figure 6. For instance, for the raceway in Table 1 we can see from Figure 6 that both $\mathbf{M}_n^{\text{for}}$ and $\mathbf{M}_n^{\text{inv}}$ can only be well conditioned if, approximately:

$$|k_p| r_1 > |n|, \quad (6.1)$$

although there are many frequencies and modes n that are ill posed for $\mathbf{M}_n^{\text{for}}$ inside this region. Specifically, the condition number $\text{cond } \mathbf{M}_n^{\text{for}}$ shows dark lines where the condition number is high. These indicate that the system is close to resonance, as small values of the boundary data lead to large values of the field. These dark lines depend on both r_2 and r_1 , however we note that: when the ratio r_2/r_1 gets closer to 1 the lines move to higher frequencies but get thicker, and when r_2/r_1 gets larger, more and more lines move from high frequencies to lower frequencies, but get thinner and thinner.

When the modal system is well conditioned, then the mode number n can be measured when using $2n$ sensors, as illustrated in the example in Section 7.1. This is a rather high demand on sensors to reach a reasonable resolution. The number of sensors needed for roller bearings, developed in Section 5, is very different as we discuss below.

Parameter	value	description
r_1	1.0 m	inner radius
r_2	1.1 m	outer radius
c_p	5000 m/s	pressure speed
c_s	3500 m/s	shear speed
ρ	7000 kg/m ³	mass density

Table 1: the parameter values that approximate a steel raceway. These parameters are used for most numerical examples.

6.1 Roller bearings at constant speed

Here our focus is to learn the Fourier coefficients of the loading profile c_n , shown in (5.4). In this section we explain an important lesson from the mathematics: the higher the rotation speed of the rollers Ω , the better conditioned the modal system becomes, and the more coefficients c_n it is possible to measure. Specifically, the lowest order coefficients $c_0, c_{-1}, c_1, c_{-2}, \dots$, become inaccessible if the speed Ω is too slow.

Let us consider an example of a steel raceway with the properties shown in Table 1. To use the prior method, we need to invert the matrices $\mathbf{M}_n^{\text{for}}$ as shown in (4.12). This inversion is only stable when (6.1) holds. If we substitute the angular frequency $\omega_m = mZ\Omega$ from (5.3) into (6.1) we obtain

$$Z|m|C > |n|, \quad \text{where } C = \Omega r_1 / \alpha,$$

note that the ω_m are the only frequencies available for constant rotation speed. Now the goal is to obtain the coefficients c_{n-mZ} from (5.9). For clarity we define $\ell = n - mZ$ and substitute $n = \ell + mZ$ in the above, and manipulating, to reach the restriction:

$$-Z(|m|C + m) < \ell < Z(|m|C - m). \quad (6.2)$$

We can measure different frequencies ω_m , which in turn implies we can choose different values for m . For each value m , the restriction (6.2) determines which values for ℓ are possible to measure. Despite this liberty, if C is small, then (6.2) will still significantly restrict all possible values for ℓ . For an example, assume that $C < 1$. For the raceway defined in Table 1 we have that $C < 1$ when $\Omega < 10$ rev/min.

Let us consider the cases:

$$-Z(C + 1) < \ell < -Z(1 - C), \quad \text{for } m = 1. \quad (6.3)$$

$$Z(1 - C) < \ell < Z(1 + C), \quad \text{for } m = -1, \quad (6.4)$$

If $C = 0.5$ then the first and second inequality above would read $-1.5Z < \ell < -0.5Z$ and $0.5Z < \ell < 1.5Z$ respectively, which together imply that $|\ell| > 0.5Z$. Larger values for $|m|$ would lead to restrictions where $|\ell|$ has to be larger. The number of rollers Z can be anything larger than 10, so that $|\ell| > 0.5Z$ would become $|\ell| > 5$. In other words, the loading coefficients c_ℓ for $\ell = -4, -3, \dots, 4$ could not be reliably measured.

The parameter C can only increase, for one fixed raceway, when the speed of rotation Ω increases. With this increased speed, more modes of the loading become available to measure by measuring elastic waves. One way to interpret this is in terms of the static limit.

6.2 Static vs dynamic regimes

In the previous section we learned that if the rollers spin too slowly then the lowest order modes of the loading $|\ell|$ can be not be robustly measured. This is because as Ω slows down, we approach the static limit. A simple way to check if we are approaching the static limit is to compare the elastic wave speed with the speed of rotation of the rollers. That is, the ratio:

$$\frac{\Omega r_1}{c_p} = \text{the roller to wave speed ratio.} \quad (6.5)$$

If the above is very small, then the rollers are almost standing still relative to the wave speed, and therefore the solution could be calculated by using static stress balance, which is known to be ill-posed [22, 26, 29], and the equations for the potentials (2.4) tend to Laplace equations which are also ill-posed [17, 21]. As discussed in the previous section, for the steel bearing in Table 1 having $c = 1$ implies that $\Omega \approx 1.05$ rad/s, which substituted into the ratio above leads to 2×10^{-4} . In conclusion, to predict the complete load due to the rollers (rotating at a constant speed) becomes well-posed if the rotation speed Ω is large enough. In practice, there are several ways around this limitation, as we explain next.

Localised defects and forces. Some important goals do not require a complete measurement of the loading through the rollers. An example of this is to detect a localised defect on, or near, the boundary in contact with the rollers. In this case, the Fourier coefficients c_ℓ , of the loading profile, for larger ℓ will be significant. These can be measured as shown in Section 7.4. Here we explain why this is possible in terms of algebra.

Suppose we are using a low frequencies ω_m which, due to the diffraction limit, implies we can only measure small values of n of the boundary conditions f_n . Turning to (5.9), and setting as an example $n = 0$, we could measure the coefficients c_{-mZ} of the loading profile, where mZ are high modes (as $Z > 10$) which are related to locating defects, as shown in Section 7.4.

7 Examples

A large number of scenarios are rigorously tested in the folder `test` of the package `ElasticWaves.jl` [10] where `MultipleScattering.jl` [11] was also used. Below we show a few examples of methods developed in this paper to both validate and illustrate our method.

In Section 7.1 we show the modes for both the forward and inverse problem and explain where they are ill-posed. Section 7.2 shows an example of generating, and predicting, a localised force on the inner raceway. There we learn that many sensors are needed to accurately predict a localised mode if we make no assumptions about the forces. If we assume there are rollers travelling at a constant speed, then as shown in Section 7.3 we can greatly reduce the

number of sensors. Finally, Section 7.4 shows an example where vibrations are due to rollers hitting a localised defect, and what can be recovered using the inverse system..

7.1 The forward and inverse modal systems

In the first sections of the paper we introduced the forward and inverse modal systems which are shown in (3.3) and (3.4). Figure 6 shows where these systems likely lead to stable solutions. Here we provide examples that the inverse problem truly recovers the boundary conditions of the forward problem. We start with a sweep over all modes and frequencies.

Boundary conditions. For every mode n and frequency ω , let us choose the boundary conditions:

$$\mathbf{f}_n = [1, 1, 0, 0]^T,$$

for the forward problem to immitate some forcing on the inner face of the raceway. We then add a uniform random 2% error and solve $\mathbf{M}_n^{\text{for}} \mathbf{a}_n = \mathbf{f}_n$ for \mathbf{a}_n . Then, to setup the inverse problem, we substitute \mathbf{a}_n in (2.4) and from these calculate the boundary data \mathbf{u}_n , the traction and displacement on the outer boundary. We then add 2% error to \mathbf{u}_n and solve $\mathbf{M}_n^{\text{inv}} \mathbf{a}_n = \mathbf{u}_n$ for \mathbf{a}_n , and finally use this \mathbf{a}_n to predict $\boldsymbol{\tau}_1$, the traction for $r = r_1$.

The heatmap of error. The error given by

$$\text{error} = |\boldsymbol{\tau}_1 - [1, 1]^T|/\sqrt{2}, \quad (7.1)$$

and is shown as a heatmap over all modes and frequencies in Figure 7 (the image on the left). We can see that most of the heatmap has an error of around 2%, meaning that most modes and frequencies lead to a well posed problem.

Visualising the modes. As explained in Section 6, the main causes that increase the error are 1) the diffraction limit and 2) resonant modes. To help visualise, we plot some modes in Figure 8, with the mode number n and wavenumber $k_p r_1$ of these modes shown by the orange spots in the heatmap on the right of Figure 7. We have chosen to use a thicker raceway with $r_1 = 1.0$ and $r_2 = 1.3$, but with the same material properties in Table 1, to better visualise the modes. The condition numbers of the forward problem for the thicker raceway is similar to the thinner raceway and is shown on the right of Figure 7.

The diffraction limit modes. The top and bottom left modes in Figure 1 are close to the diffraction limit, meaning the potentials approximately obey Laplace’s equation. Notably, solutions to Laplace’s equation are also solutions to a diffusion equation, where any source smoothly dissipates as it moves away from its origin. Solutions to the Laplacian are known to be ill posed and are essentially the same as the diffraction limit [17, 21].

Near resonant modes. The two images in the middle column of Figure 8 illustrate near resonant modes. That is the pressure on both boundaries is near zero, while the pressure away from the boundaries grows. This is why small errors in the boundaries lead to large errors in the fields for these modes.

Well-posed modes. The top and bottom right modes shown in Figure 8 are well posed, as both phase information is still present, and the pressure is not small on all boundaries.

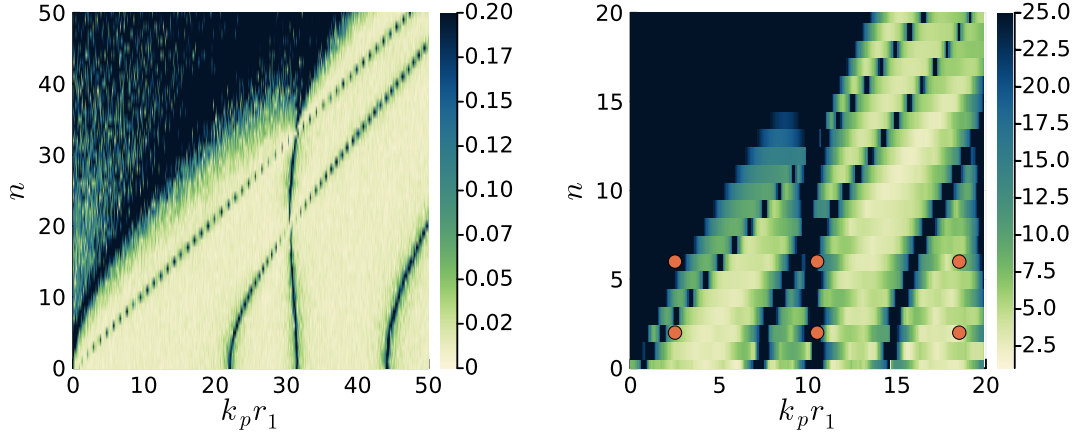


Figure 7: On the left is the error in the traction τ_1 , shown by (7.1), with τ_1 predicted by the inverse problem after adding 2% error to all boundary data. Table 1 shows the parameters used. The right shows the condition number of $\mathbf{M}_n^{\text{for}}$ but for a thicker raceway: $r_1 = 1.0$ and $r_2 = 1.3$, which is easier to visualise the modes, where the modes are shown in Figure 8 for the parameters of the orange spots.

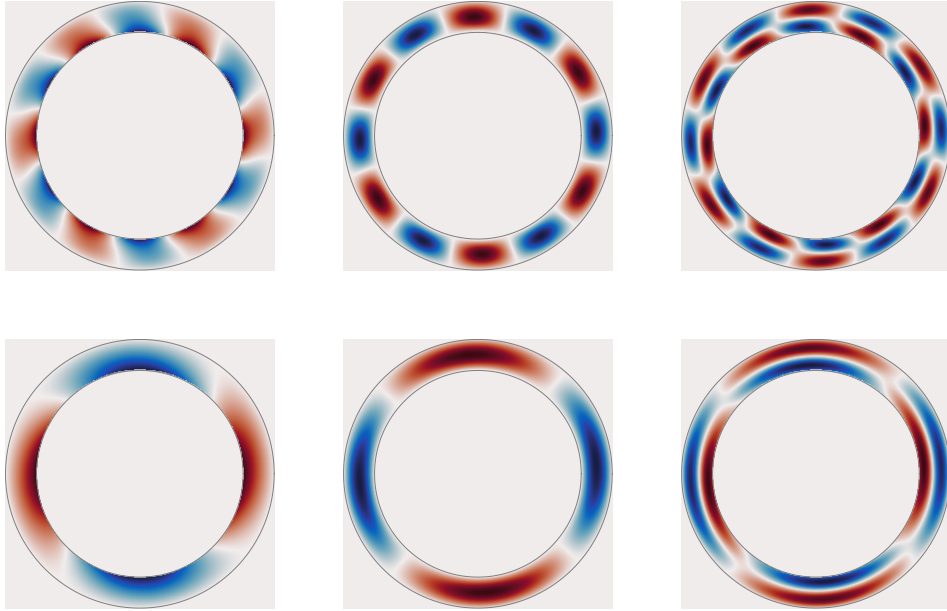


Figure 8: Above shows the real part of the pressure field from solving the forward system (3.3) for the modes $n = 2$ or 6 , and $k_p r_1 = 2.5, 10.5$, or 18.5 . Red (blue) is positive (negative) pressure, while white is no pressure. The colour scaling is different for each mode, but the outer boundary is always traction-free so it is white. The outer radius $r_2 = 1.3$ which is easier to visualise than $r_1 = 1.1$. The chosen modes are shown as an orange scatter on Figure 7. Middle plots show resonance so large field inside for small boundary data.

7.2 A localised force on the boundary

In the previous section we saw that the inverse problem in general works, when outside of resonance of the low frequency limit. Here we show an example where although the inverse problem is well posed, you would need many Fourier modes to converge, and therefore many sensors. The material parameters and dimensions of the bearing used in these simulations are laid out in Table 1. This section acts as motivation for using the prior method developed in Section 4.

Boundary conditions and method. Consider a sharp Gaussian force applied to the inner boundary given by

$$f(\theta) = \frac{1}{\sigma\sqrt{2\pi}} e^{-\frac{(\theta-\pi)^2}{2\sigma^2}}, \quad (7.2)$$

where $\sigma = 0.1$. For the forward model we use the boundary conditions

$$\boldsymbol{\tau}^1 = f(\theta)\hat{\mathbf{r}} \quad \text{and} \quad \boldsymbol{\tau}^2 = \mathbf{0},$$

which for one fixed frequency ω leads to the modal system

$$\mathbf{M}_n^{\text{for}} \mathbf{a}_n = [f_n, 0, 0, 0]^T, \quad (7.3)$$

where f_n is the n th coefficient of the Fourier series expansion of the forcing (7.2). A large number of coefficients f_n are needed to accurately represent $f(\theta)$, which is why this example will need many sensors to obtain a good resolution. Solving Equation (7.3) for each mode n gives a solution to the forward problem.

Just as before, to setup the inverse problem, we use the forward problem to predict the displacement \mathbf{u}_n on the outer boundary $r = r_2$, and then add 1% error to \mathbf{u}_n and then solve the inverse modal problem (3.4) for \mathbf{a}_n . With \mathbf{a}_n we then predict the traction $\boldsymbol{\tau}_1$ and compare it with the true traction. The results for the frequency $k_p r_1 = 65$ are shown in Figure 9 where the ribbon is 10 the standard deviation from solving this problem many times each with a different error added.

Results. From the thickness of the ribbon in the plot on the right of Figure 9 we can see that the problem is well posed for $k_p r_1 = 65$. This relatively high frequency avoids most resonances, and allows us to recover very high Fourier modes by avoiding the diffraction limit. However, the number of sensors needed to reach a relative error less than 20% is around 25, as can be seen from the graph on the left of Figure 9.

Clearly a Fourier series representation $f(\theta) = \sum_n f_n e^{in\theta}$ is not the best choice for a localised force. However, by making assumptions about what led to the force, or more generally the boundary conditions, we can use many other representations. For example, we can assume the traction is due to contact with rollers bearings rotating at a constant speed, as we do in the next section.

7.3 Recovering the loading profile for rollers

In this section we show an example of predicting the loading on the bearings by using the methods developed in Section 5.1. That is, we assume that the rollers are rotating at a constant speed.

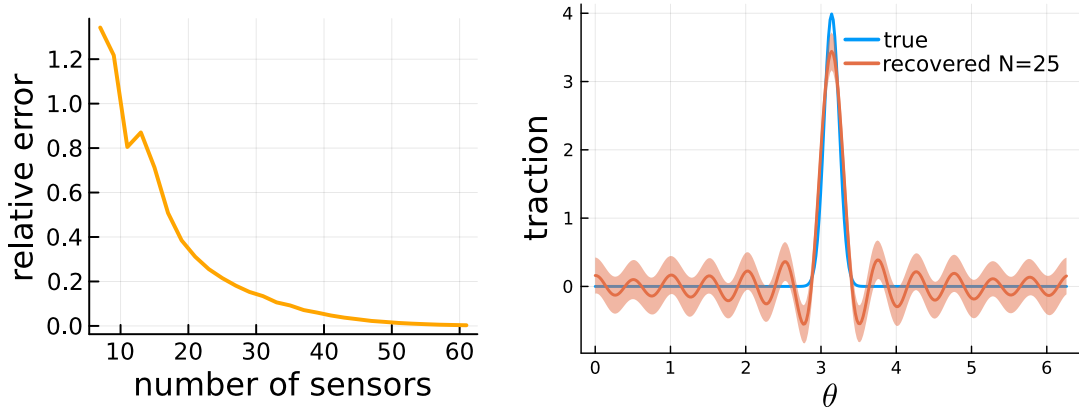


Figure 9: The left shows the convergence of solving the inverse problem, with 1% error added to its boundary conditions, to recover the force shown on the right. As the number of sensors increases so does the number of Fourier modes n that can be recovered. The right shows the forcing $f(\theta)$ given by (7.2) compared with the mean predicted force from the inverse problem for $k_p r_1 = 65$, using 25 sensors, and with a 10 standard deviation ribbon to show the uncertainty.

Stribeck boundary condition. To create a realistic boundary conditions for the inverse problem we use the Stribeck equation for the loading profile of roller bearings [13], it is given by

$$L(\theta) = L_0 \left(1 - \frac{1}{2\epsilon}(1 - \cos \theta) \right)^{10/9}, \quad (7.4)$$

where ϵ is called the load distribution factor. This parameter determines the loading zone, that is, the region where the load is being applied. For a radial loading, it is related to the loading region through:

$$\epsilon = \frac{1}{2} (1 - \cos(\varphi/2)) \quad (7.5)$$

where φ is the angular extent of the loading zone.

For the numerical simulations, we used $L_0 = 1$ and $\epsilon = 0.5$, which implies a loading zone of angular length of $\varphi = \pi$. Figure 1 shows this Stribeck loading profile. The other parameters used for this section are shown in Table 2, where we use a thicker raceway with thickness 1m to make the plots below easier to see.

Data from the forward problem. Like the previous sections, we create the boundary data for the inverse problem, represented by \mathbf{y}^{inv} in (4.14), by solving the forward problem. In this section, for the forward problem we used the loading (7.4), from which the c_n coefficients in (5.4) can be calculated, which then lead to the Fourier modes f_n shown in (5.5) which we use for the boundary conditions of the forward problem. Again we assume the outer boundary $r = r_2$ is traction free with $\boldsymbol{\tau}_1 = \mathbf{0}$.

Parameter	value	description
r_1	2.5 m	inner radius
r_2	3.5 m	outer radius
c_p	5000 m/s	pressure speed
c_s	3500 m/s	shear speed
ρ	7800 kg/m ³	mass density
Ω	2000 rpm	rotation speed

Table 2: Parameter values used for numerical simulations in Section 7.3.

After solving the forward problem, we can then calculate \mathbf{y}^{inv} from (3.9) for a chosen number of sensors, where \mathbf{a} is given by solving the forward problem, and \mathbf{E} is composed of the modal matrices for the inverse problem.

Results. To solve the inverse problem using the prior method we can follow the steps shown at the end of Section 5.1. The result is that at least 4 sensors are needed to recover the loading profile, when adding 4% noise, as shown by the Figure 1 in the introduction, which shows the predicted pressure distribution, and Figure 10 which shows the predicted displacement. Figure 11 shows a more quantitative view with just the predicted loading profile $L(\theta)$ when using 4 and 7 sensors, shown against the exact loading profile used. When using 4 or 7 sensor we are only trying to recover the Fourier coefficients $c_{-2}, c_{-1}, c_0, c_1,$ and c_2 . When using 4 sensors there is a reasonably large error because the higher Fourier coefficients, which are ignored, make a substantial contribution to the Stribeck equation shown in Figure 11. With only 4 sensors, the ignored higher Fourier coefficients are treated liked an add error (20%), which explains the error in recovering the coefficients $c_{-2}, c_{-1}, c_0, c_1,$ and c_2 . When using 7 sensors, we are able to differentiate the modes associate with c_{-3}, c_3 from the lower modes.

7.4 Localised defect in a roller bearing

As our final example, we consider a a localised defect on, or near, the boundary in contact with the rollers. A schematic is shown on the right of Figure 12.

Defects and slow rotation. In the previous example we showed how a smooth loading profile can be predicted with only a few sensors by using the prior method, together with a Fourier series expansion of the loading profile, as shown in Section 5.1. To predict the loading profile, the rollers need to rotate fast enough, as discussed in Section 6.2. If the rollers are rotating slower, then we can only predict the higher Fourier coefficients c_ℓ for larger ℓ , which are associated to localised defects, as we illustrate in this example.

Use the inverse modal system. Consider the inside raceway with two localised defects which we assume leads to a loading profile shown by the orange dashed curve on the left of Figure 12. This time, rewriting the loading profile in terms of a Fourier series, as done in Section 5.1, does not help because the Fourier series will converge very slowly. So instead, just to illustrate, we just directly solve the system (3.9) using the inverse modal system (3.4) and boundary data \mathbf{y}^{inv} solely from the outer boundary.

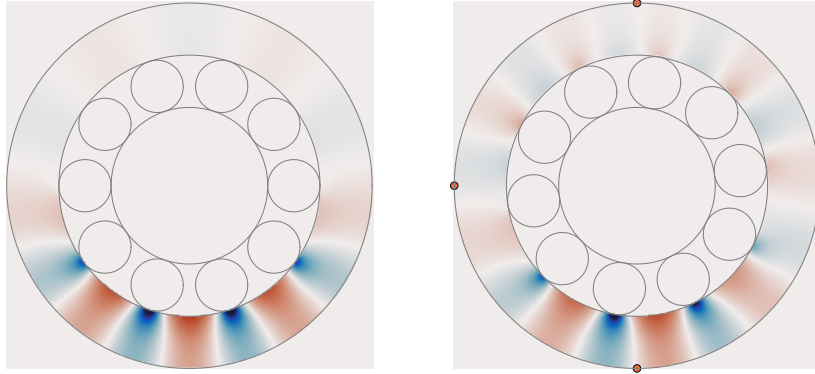


Figure 10: True radial displacement on the left for one snapshot in time when using the Stribeck equation (7.4) and the properties in Table 2. The snapshot in time is a result of taking a Fourier transform over all frequencies. The right shows the predicted radial displacement when using only 4 sensors shown as orange spots. The sensors measure displacement, and the outer boundary is stress free. We can see that despite being stress free on the boundary $r = r_2$, the displacement is not zero there. The recovery is not perfect as 4% noise is added, and limit sensors imply limited Fourier modes are recovered.

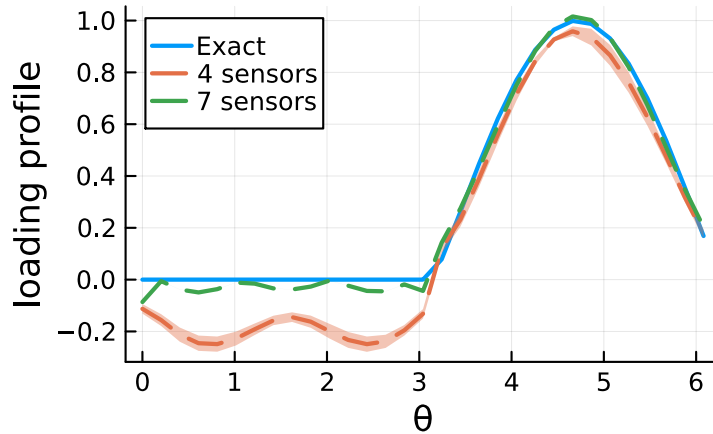


Figure 11: The blue curve shows the Stribeck equation for the loading of rollers given in (7.4), the orange is prior method with 4 sensors and modes -2:2 and 4% added error to boundary data, other than 20% error caused from lacking Fourier mode. Also added 4% white noise error on top. Green is also modes -2:2 and 4% added error, but with 7 sensors able to resolve and ignore higher Fourier modes.

We return to using the parameters in Table 1, as these more closely match real applications,

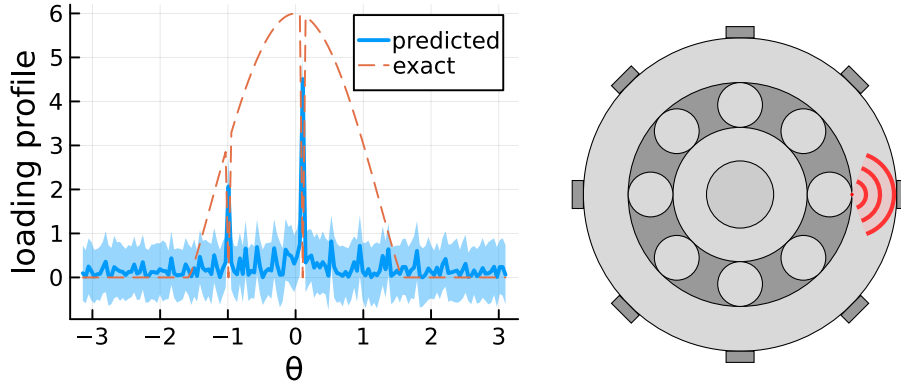


Figure 12: The right is an illustration of elastic waves being emitted when a roller hits a defect on the raceway. The left shows the loading profile (orange and dashed) with two sharp drops in pressure due to the presence of two defects on the inner boundary. The blue curves show the absolute value of the predicted loading profile when measuring the Fourier coefficients of the boundary data \mathbf{u}_n for $n = -6, -5, \dots, 6$ where 2% error was added. The rollers are rotating at a rate of $\Omega = 120$ rpm and the properties used for the raceway are shown in Table 1.

but use now a slower rotation speed of the rollers $\Omega = 120$ rpm. As discussed in Section 6.1, for slow rotation speeds there are restrictions on which of the Fourier coefficients c_ℓ , of the loading profile, can be measured.

What can be measured. Each frequency ω_m gives access to a range of values for ℓ . For this example we use the frequencies $m = 1, 2, \dots, 5$ and for each solve (3.9) for \mathbf{a} , and then predict the inner traction $\boldsymbol{\tau}_1$. From $\boldsymbol{\tau}_1$, and depending on the choice of m , we then estimate some of the coefficients c_ℓ of the loading profile by using (5.5). By combining all the predicted coefficients c_ℓ from all five frequencies ω_m we then predict the absolute value loading profile shown by the blue curve in Figure 12. We have shown the absolute value for visual clarity, as we can more clearly see that the blue and orange spikes match up perfectly.

Clearly, Figure 12 shows that we are able to both locate the defects, and determine their magnitude, at least in terms of the pressure difference, by directly solving the inverse problem.

Envelope analysis. There is a method commonly used to detect localised defects called *envelope analysis* [37]. Here we only make a brief comment on how this method is connected to the work in this paper.

For the example in this section, we are not able to recover the first modes c_0 , c_{-1} , or c_1 of the loading profile. However, these modes are not small, and therefore do make a contribution to our boundary data. They in fact act like an error term. For example, for the frequency ω_m , the coefficient c_0 contributes to $f_{mZ}(\omega_m)$ of the boundary data as shown in (5.5). If we have less than $m \times Z$ sensors, and attempt to calculate a Fourier series of the loading data $y(\theta, \omega_m)$, then the mode of $f_{mZ}(\omega_m)$ will be mixed in with the other modes

$f_n(\omega_m)$, for $|n| < m \times Z$, and lead to errors for these modes. This error could be avoided if the function $y(\theta, \omega_m)$ was first smoothed in θ before calculating the Fourier modes, as the smoothening would remove the higher modes such as $f_{mZ}(\omega_m)$. We believe this can be linked with the smoothening in time used in Envelope Analysis, though this deserves a more lengthy analysis elsewhere.

8 Conclusions

In this paper we have shown how to model elastic waves confined within a hollow thick walled cylinder with symmetry along the axis. As discussed in Section 2, the dynamics of these waves captures the dominant vibrations within a raceway. By deriving simple systems for the modes, we provided tools to better understand and quickly solve for these elastic waves. A detailed outline of the paper's content is given at the end of Section 1.

Results. The main results are how to: 1) model waves, 2) use prior assumptions about the boundary conditions, and 3) determine what it is, and is not, possible to predict the traction or displacement within the raceway. Notably, in Section 6, we show that solving for the elastic waves becomes ill-posed when hitting a resonant frequency or near the diffraction limit. These results hold for any transfer path of the signal. For roller bearings we demonstrate that if the rotation speed is slow, then it is only possible to predict localised contact forces. Extended, or smooth, contact forces lead to ill-posed problems for elastic waves.

Modelling - raceways. Our models lay the foundation for many future avenues. For instance, instead of considering waves which are just confined in the raceway, as shown by Figure 8, the boundary conditions can be adjusted to let waves leak out towards the rollers or the oil. Additionally, the raceway's bolted supports can be incorporated in the boundary conditions by assuming that waves dissipate through these bolts and are not reflected back into the raceway.

Modelling - bearings. It is also possible to extend the models to consider bearings that do not have axial symmetry, such as ball bearings or steeply inclined tapered roller bearings. Further extensions could account for the slip and slide of roller bearings [36] which lead to transient waves with a high-frequency content. Incorporating these phenomena into the models as more elaborate priors would lead to more accurate predictions.

Inverse problem - uncertainty. To develop robust predictions, and methods to determine defects, uncertainty needs to be accounted for [20]. A first step in this direction is to consider the boundary data to be samples of a distribution, and also to consider that priors, as discussed in Section 4.1, are also distributions. This would help properly account for roller bearings slipping, or fluid interaction in journal bearings.

Detect localised defects. In industrial applications, it is common to have very few sensors per bearing, which limits the diagnostic methods available. With only a few sensors, defect detection often relies on monitoring the amplitude of specific frequencies, such as the ball pass frequencies, to identify defects. Can we rely on these methods? The models in this paper provide a clear path to address this question: imagine continually measuring the vibration of a bearing. When a change occurs, we can assume it is due to a localised defect with an

unknown position and size. By adopting a Bayesian approach, we can then estimate the defect size by marginalising over its possible positions. This approach would clarify how robust current methods are and lead to more reliable, physics-based diagnostic methods to detect defects.

A Entries of M_n^{for} and M_n^{inv}

Equation (3.3) may be written as

$$\begin{pmatrix} P_1^{(n)}(r_1) & P_2^{(n)}(r_1) & P_3^{(n)}(r_1) & P_4^{(n)}(r_1) \\ S_1^{(n)}(r_1) & S_2^{(n)}(r_1) & S_3^{(n)}(r_1) & S_4^{(n)}(r_1) \\ P_1^{(n)}(r_2) & P_2^{(n)}(r_2) & P_3^{(n)}(r_2) & P_4^{(n)}(r_2) \\ S_1^{(n)}(r_2) & S_2^{(n)}(r_2) & S_3^{(n)}(r_2) & S_4^{(n)}(r_2) \end{pmatrix} \begin{pmatrix} a_n \\ b_n \\ c_n \\ d_n \end{pmatrix} = \begin{pmatrix} -p_n^1 \\ -s_n^1 \\ p_n^2 \\ s_n^2 \end{pmatrix}$$

where,

$$\begin{aligned} P_1^{(n)}(r) &= -\frac{\rho}{r^2} (2c_s^2 k_p r J_{n-1}(k_p r) + (r^2 \omega^2 - 2c_s^2 n(n+1)) J_n(k_p r)) \\ P_2^{(n)}(r) &= -\frac{\rho}{r^2} (2c_s^2 k_p r H_{n-1}^{(1)}(k_p r) + (r^2 \omega^2 - 2c_s^2 n(n+1)) H_n^{(1)}(k_p r)) \\ P_3^{(n)}(r) &= \frac{i\rho c_s^2 n}{r^2} (k_s r J_{n-1}(k_s r) - 2J_n(k_s r) - k_s r J_{n+1}(k_s r)) \\ P_4^{(n)}(r) &= \frac{i\rho c_s^2 n}{r^2} (k_s r H_{n-1}^{(1)}(k_s r) - 2H_n^{(1)}(k_s r) - k_s r H_{n+1}^{(1)}(k_s r)) \\ S_1^{(n)}(r) &= \frac{i\rho c_s^2 n}{r^2} (k_p r J_{n-1}(k_p r) - 2J_n(k_p r) - k_p r J_{n+1}(k_p r)) \\ S_2^{(n)}(r) &= \frac{i\rho c_s^2 n}{r^2} (k_p r H_{n-1}^{(1)}(k_p r) - 2H_n^{(1)}(k_p r) - k_p r H_{n+1}^{(1)}(k_p r)) \\ S_3^{(n)}(r) &= \frac{\rho}{r^2} (2c_s^2 k_s r J_{n-1}(k_s r) + (r^2 \omega^2 - 2c_s^2 n(n+1)) J_n(k_s r)) \\ S_4^{(n)}(r) &= \frac{\rho}{r^2} (2c_s^2 k_s r H_{n-1}^{(1)}(k_s r) + (r^2 \omega^2 - 2c_s^2 n(n+1)) H_n^{(1)}(k_s r)) \end{aligned}$$

Equation (3.4) may be written as

$$\begin{pmatrix} U_{r,1}^{(n)}(r_2) & U_{r,2}^{(n)}(r_2) & U_{r,3}^{(n)}(r_2) & U_{r,4}^{(n)}(r_2) \\ U_{\theta,1}^{(n)}(r_2) & U_{\theta,2}^{(n)}(r_2) & U_{\theta,3}^{(n)}(r_2) & U_{\theta,4}^{(n)}(r_2) \\ P_1^{(n)}(r_2) & P_2^{(n)}(r_2) & P_3^{(n)}(r_2) & P_4^{(n)}(r_2) \\ S_1^{(n)}(r_2) & S_2^{(n)}(r_2) & S_3^{(n)}(r_2) & S_4^{(n)}(r_2) \end{pmatrix} \begin{pmatrix} a_n \\ b_n \\ c_n \\ d_n \end{pmatrix} = \begin{pmatrix} u_n^{(r)} \\ u_n^{(\theta)} \\ p_n^2 \\ s_n^2 \end{pmatrix}$$

where,

$$\begin{aligned}
U_{r,1}^{(n)}(r) &= \frac{k_p}{2} (J_{n-1}(k_p r) - J_{n+1}(k_p r)), & U_{r,2}^{(n)}(r) &= \frac{k_p}{2} \left(H_{n-1}^{(1)}(k_p r) - H_{n+1}^{(1)}(k_p r) \right), \\
U_{r,3}^{(n)}(r) &= \frac{in}{r} J_n(k_s r), & U_{r,4}^{(n)}(r) &= \frac{in}{r} H_n^{(1)}(k_s r), & U_{\theta,1}^{(n)}(r) &= \frac{in}{r} J_n(k_p r), & U_{\theta,2}^{(n)}(r) &= \frac{in}{r} H_n^{(1)}(k_p r) \\
U_{\theta,3}^{(n)}(r) &= \frac{-k_s}{2} (J_{n-1}(k_s r) - J_{n+1}(k_s r)), & U_{\theta,4}^{(n)}(r) &= \frac{-k_s}{2} \left(H_{n-1}^{(1)}(k_s r) - H_{n+1}^{(1)}(k_s r) \right).
\end{aligned}$$

B Derivation of traction components

In this section we show how to derive equations (2.7) and (2.8). We begin by specifying the form of the stress tensor. In our case, since the material we are considering is homogeneous and isotropic the desired form is given by equation (2.5). Using (2.5), we obtain the following expressions for σ_{rr} and $\sigma_{r\theta}$ in terms of the displacement \mathbf{u}

$$\sigma_{rr} = \lambda \left(\frac{\partial u_r}{\partial r} + \frac{1}{r} \left(\frac{\partial u_\theta}{\partial \theta} + u_r \right) \right) + 2\mu \frac{\partial u_r}{\partial r}, \quad \sigma_{r\theta} = \frac{\mu}{r} \left(\frac{\partial u_r}{\partial \theta} + r \frac{\partial u_\theta}{\partial r} - u_\theta \right). \quad (\text{B.1})$$

We will deduce both equations in turn, beginning with σ_{rr} . Firstly, note that (B.1)₁ may be rewritten as

$$\sigma_{rr} = (\lambda + 2\mu) \nabla \cdot \mathbf{u} - \frac{2\mu}{r} \left(\frac{\partial u_\theta}{\partial \theta} + u_r \right). \quad (\text{B.2})$$

From $\mathbf{u} = \nabla \phi + \nabla \times (\psi \hat{\mathbf{z}})$ we see that $\nabla \cdot \mathbf{u} = \nabla^2 \phi = -k_p^2 \phi$, hence

$$\sigma_{rr} = -k_p^2 (\lambda + 2\mu) \phi - \frac{2\mu}{r} \left(\frac{\partial u_\theta}{\partial \theta} + u_r \right).$$

Substituting (2.1) into (2.2) leads to

$$\frac{1}{r} \left(\frac{\partial u_\theta}{\partial \theta} + u_r \right) = -k_p^2 \phi - \frac{\partial^2 \phi}{\partial r^2} - \frac{\partial}{\partial r} \left(\frac{1}{r} \frac{\partial \psi}{\partial \theta} \right),$$

which itself substituting into σ_{rr} above leads to

$$\sigma_{rr} = -\lambda k_p^2 \phi + 2\mu \left(\frac{\partial^2 \phi}{\partial r^2} + \frac{\partial}{\partial r} \left(\frac{1}{r} \frac{\partial \psi}{\partial \theta} \right) \right). \quad (\text{B.3})$$

Finally using (2.3) we deduce $\lambda = \rho(c_p^2 - 2c_s^2)$ which together with $\omega = c_p k_p$ substituted above leads to (2.7).

To simplify $\sigma_{r\theta}$ in (B.1)₂ first we rewrite it in the form

$$\sigma_{r\theta} = \mu (\nabla \times \mathbf{u}) \cdot \hat{\mathbf{z}} - \frac{2\mu}{r} \left(u_\theta - \frac{\partial u_r}{\partial \theta} \right).$$

Now, from (2.1) and (2.2), we have $(\nabla \times \mathbf{u}) \cdot \hat{\mathbf{z}} = -\nabla^2 \psi = k_s^2 \psi$, which substituted above leads to

$$\sigma_{r\theta} = \mu k_s^2 \psi - \frac{2\mu}{r} \left(u_\theta - \frac{\partial u_r}{\partial \theta} \right).$$

Using (2.1) and (2.2) we find that

$$\frac{1}{r} \left(u_\theta - \frac{\partial u_r}{\partial \theta} \right) = k_s^2 \psi + \frac{\partial^2 \psi}{\partial r^2} - \frac{\partial}{\partial r} \left(\frac{1}{r} \frac{\partial \phi}{\partial \theta} \right),$$

which substituted into $\sigma_{r\theta}$ above leads to

$$\sigma_{r\theta} = -\mu k_s^2 \psi - 2\mu \left(\frac{\partial^2 \psi}{\partial r^2} - \frac{\partial}{\partial r} \left(\frac{1}{r} \frac{\partial \phi}{\partial \theta} \right) \right),$$

which is the same as (2.8) after using $\mu = \rho c_s^2$ and $\omega = c_s k_s$.

C The Diffraction Limit

One cause of the modal system becoming ill-posed, as shown in Section 6, is due to the diffraction limit [30]. Below we provide an approximate formula based classical argument of the diffraction limit to easily determine when the system is ill-posed.

Instead of solving a boundary value problem, we consider a simpler case of determining the amplitude A and B of two point sources on the boundary $r = r_1$. These in sense imitate to forcing on the boundary. The field emitted by these sources is given by

$$\phi_{\text{src}} = \frac{i}{4} \left(AH_0^{(1)}(k_p |\mathbf{r} - \mathbf{r}^{(1)}|) + BH_0^{(1)}(k_p |\mathbf{r} - \mathbf{r}^{(2)}|) \right), \quad (\text{C.1})$$

with $\mathbf{r}^{(1)}$ and $\mathbf{r}^{(2)}$ representing the position of the first and second point source respectively.

Now we ask, can we tell the different between these two sources by measuring the field on boundary $r = r_2$? That is, can we distinguish between a source at $\mathbf{r}^{(1)}$ from $\mathbf{r}^{(2)}$? As we want to determine the maximum amount of information available we consider that we have access to the field everywhere on the boundary $r = r_2$. To achieve this it is convenient to use the origin \mathbf{O}_2 , the midpoint of the chord connecting the two sources. Then we can use Graff's addition theorem [1, 34] to rewrite (C.1) as

$$\phi_{\text{src}} = \frac{i}{4} \sum_n \left(AJ_{-n}(k_p r_0) H_n^{(1)}(k_p r) + BJ_n(k_p r_0) H_n^{(1)}(k_p r) \right) e^{in\theta}, \quad (\text{C.2})$$

where r_0 is the horizontal distance from \mathbf{O}_2 to each source, r is the distance from \mathbf{O}_2 to some observation point on the outer boundary, and θ is the angle of the observation point from the source at $\mathbf{r}^{(1)}$, this is illustrated in Figure 13.

To reach a simple approximate formula, we consider the limit when the sources are close $k_p r_0 \rightarrow 0$, and also evaluate (C.2) in the far field $k_p r \rightarrow \infty$. The information count should

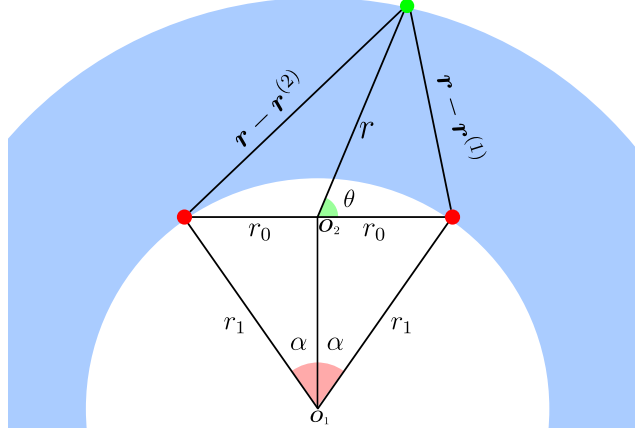


Figure 13: Illustration of Graff's addition theorem. r_0 is the distance from \mathbf{O}_2 to each source, r is the distance from \mathbf{O}_2 to some observation point on the outer boundary, and θ is the angle of the observation point from the source at $\mathbf{r}^{(1)}$. The angles α are needed to relate these sources to Fourier modes later.

not significant change in the far-field, but it does simplify the field. Taking these asymptotic limits and retaining up to $\mathcal{O}(k_p^2 r_0^2)$, while keeping only the leading for $k_p r \rightarrow \infty$, leads to:

$$\phi_{\text{src}} = \frac{1+i}{8\sqrt{\pi k_p r}} e^{ik_p r} [2(A+B) + 2i(A-B)k_p r_0 \cos \theta - (A+B)(k_p r_0 \cos \theta)^2]. \quad (\text{C.3})$$

Now to distinguish between the sources we need to determine r_0 by measuring the above. We can further simplify this by specialising to the case where the boundary data is smooth, which will lead to a lower bound on what can be measured. In this case, we consider that B is a smooth function of r_0 such that asymptotically:

$$B = A + \frac{\beta}{2} r_0^2,$$

which substituted into (C.3) leads to:

$$\phi_{\text{src}} = \frac{1+i}{8\sqrt{\pi k_p r}} e^{ik_p r} [4A + r_0^2 \beta - 2A(r_0 k_p \cos \theta)^2]. \quad (\text{C.4})$$

The β term can be anything, but will change from a negative and positive value as the $\mathbf{r}^{(2)}$ changes. When β has the same sign of A it will make it easier to determine r_0 , and when the signs are opposite it will make it harder to determine r_0 . To reach a simple approximation we take $\beta = 0$. Then, to resolve the difference between the sources at $\mathbf{r}^{(1)}$ and $\mathbf{r}^{(2)}$ we need to easily measure r_0 , which implies that the quadratic term r_0^2 in (C.4) needs to be greater or equal to the leading term, that is

$$|k_p r_0 \cos \theta|^2 \geq 2 \quad (\text{C.5})$$

which is guaranteed to hold if $|k_p r_0| \geq \sqrt{2}$.

The main method of the paper uses a modal Fourier decomposition (2.4) to solve for elastic waves. For these, the level of detail of the boundary data increases with the Fourier order n . The minimal level of detail captured by order n is the distance on the boundary between a trough and a crest which is equal to $\theta = r_1 |n|/\pi$. From Figure 13 we see that this leads to the choice $2\alpha = \pi/|n|$ and

$$r_0 = r_1 \sin\left(\frac{\pi}{2|n|}\right) \approx \frac{\pi r_1}{2|n|}, \quad (\text{C.6})$$

where the approximation is accurate for $|n| > 1$. Substituting the above into $|k_p r_0| \geq \sqrt{2}$ yields the following useful result

$$\pi k_p r_1 \geq \sqrt{8}|n|. \quad (\text{C.7})$$

Figure 14 shows when equality holds in the above superimposed on the condition number plot in Figure 6. It is clear that the limit loosely indicates where we begin to lose precision due to an ill-condition system. In reality, it is clear, that the true bound depends on more factors than those found in Equation (C.7).

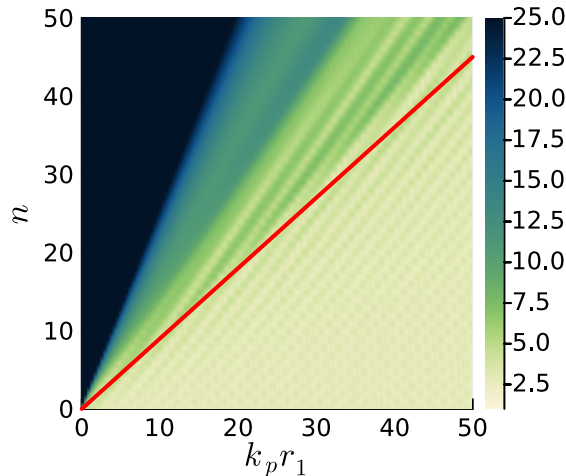


Figure 14: Figure shows the condition number plot from Figure 6 with the diffraction limit in Equation (C.7) plotted on top in red. The diffraction limit gives a rough idea of when the inverse problem is well-posed; though it only a loose idea as we have not taken account of multiple scattering events and have performed the calculation in free space.

References

- [1] Milton Abramowitz et al. *Handbook of Mathematical Functions with Formulas, Graphs, and Mathematical Tables*. ninth Dover printing, tenth GPO printing. New York: Dover, 1964.

- [2] Jan D. Achenbach. *Wave Propagation in Elastic Solids*. Amsterdam: Elsevier Science, 2005.
- [3] Miba AG. *A Miba Industrial Tilting Pad Journal Bearings*. 2024. URL: <https://www.miba.com/en/product-areas/industrial-bearings/tilting-pad-journal-bearing>.
- [4] Jérôme Antoni. “The spectral kurtosis: a useful tool for characterising non-stationary signals”. In: *Mechanical systems and signal processing* 20.2 (2006), pp. 282–307.
- [5] J.R. Barber. *Contact Mechanics*. Cham, Switzerland: Springer, 2018. URL: <https://books.google.co.uk/books?id=4GNLDwAAQBAJ>.
- [6] Alan Champneys et al. “Characterising Spectral Anomalies in Rotating Machine Sensors”. In: *Mathematics in Industry Reports* (2021).
- [7] David Colton et al. “The linear sampling method in inverse electromagnetic scattering theory”. In: *Inverse Problems* 19.6 (2003), S105–S137.
- [8] Mark J Eaton et al. “Towards improved damage location using acoustic emission”. In: *Proceedings of the Institution of Mechanical Engineers, Part C: Journal of Mechanical Engineering Science* 226.9 (2012), pp. 2141–2153.
- [9] Phillip L. Gould et al. *Introduction to Linear Elasticity*. Cham: Springer, 2018.
- [10] AL Gower et al. *ElasticWaves.jl: A Julia library to calculate propagation and scattering of elastic waves*. 2024. URL: <https://github.com/JuliaWaveScattering/ElasticWaves.jl/tree/v0.1.0>.
- [11] AL Gower et al. *MultipleScattering.jl: A Julia library for simulating, processing, and plotting multiple scattering of waves*. 2020. URL: <https://github.com/JuliaWaveScattering/MultipleScattering.jl>.
- [12] C.U. Grosse et al. *Acoustic Emission Testing: Basics for Research – Applications in Engineering*. Springer Tracts in Civil Engineering. Springer International Publishing, 2021. URL: <https://books.google.co.uk/books?id=EYk4EAAAQBAJ>.
- [13] T.A. Harris. *Rolling Bearing Analysis*. A Wiley-interscience publication. Wiley, 2001. URL: <https://books.google.co.uk/books?id=Pt9SAAAAMAAJ>.
- [14] Edward Hart et al. “Wind Turbine Main-Bearing Loading and Wind Field Characteristics”. In: *Wind Energy* 22.11 (2019), pp. 1534–1547.
- [15] Ian Howard. “A Review of rolling element bearing vibration "Detection, Diagnosis and Prognosis“”. In: (Oct. 1994).
- [16] Tomasz Hrycak et al. “Increased stability in the continuation of solutions to the Helmholtz equation”. In: *Inverse Problems* 20.3 (2004), pp. 697–712.
- [17] Victor Isakov. *Inverse Problems for Partial Differential Equations*. Springer, 2017, pp. 80–84.

- [18] S Janjarasjitt et al. “Bearing condition diagnosis and prognosis using applied nonlinear dynamical analysis of machine vibration signal”. In: *Journal of Sound and Vibration* 317 (2008), pp. 112–126.
- [19] Matthew R Jones et al. “A Bayesian methodology for localising acoustic emission sources in complex structures”. In: *Mechanical Systems and Signal Processing* 163 (2022), p. 108143.
- [20] Matthew R Jones et al. “Bayesian localisation of acoustic emission sources for wind turbine bearings”. In: *Health monitoring of structural and biological systems XV*. Vol. 11593. SPIE. 2021, pp. 443–453.
- [21] Jari Kaipio et al. *Statistical and computational inverse problems*. Vol. 160. Springer Science & Business Media, 2006.
- [22] D.B. Ingham L. Marin L. Elliott et al. “Boundary Element Regularisation Methods for Solving the Cauchy Problem in Linear Elasticity”. In: *Inverse Problems in Engineering* 10.4 (2002), pp. 335–357. eprint: <https://doi.org/10.1080/1068276021000004698>. URL: <https://doi.org/10.1080/1068276021000004698>.
- [23] A W Lees et al. “Model-based identification of rotating machines”. In: *Mechanical Systems and Signal Processing* 23.6 (2009), pp. 1884–1893.
- [24] Arthur W Lees. *Vibration problems in machines: diagnosis and resolution*. CRC Press, 2020.
- [25] Guo-Yang Li et al. “An ultrasonic method to measure stress without calibration: The angled shear wave method”. In: *The Journal of the Acoustical Society of America* 148.6 (2020), pp. 3963–3970.
- [26] L Marin et al. “Boundary element method for the Cauchy problem in linear elasticity”. In: *Engineering Analysis with Boundary Elements* 25.9 (2001), pp. 783–793. URL: <https://www.sciencedirect.com/science/article/pii/S0955799701000625>.
- [27] Jerrold E Marsden et al. *Mathematical foundations of elasticity*. Courier Corporation, 2012.
- [28] Paul A Martin. *Multiple scattering: interaction of time-harmonic waves with N obstacles*. 107. Cambridge University Press, 2006.
- [29] T.J. Martin et al. “An inverse method for finding unknown surface tractions and deformations in elastostatics”. In: *Computers & Structures* 56.5 (1995). Boundary Element Method, pp. 825–835. URL: <https://www.sciencedirect.com/science/article/pii/0045794995000115>.
- [30] AA Maznev et al. “Upholding the diffraction limit in the focusing of light and sound”. In: *Wave Motion* 68 (2017), pp. 182–189.
- [31] P.D. McFadden et al. “Model for the vibration produced by a single point defect in a rolling element bearing”. In: *Journal of Sound and Vibration* 96.1 (1984), pp. 69–82.

- [32] P.D. McFadden et al. “The vibration produced by multiple point defects in a rolling element bearing”. In: *Journal of Sound and Vibration* 98.2 (1985), pp. 263–273.
- [33] Tobias Souza Morais et al. “Rotating machinery health evaluation by modal force identification”. In: *Inverse Problems in Science and Engineering* 28.5 (2020), pp. 695–715.
- [34] K. K. Napal et al. “Effective T-matrix of a cylinder filled with a random two-dimensional particulate”. In: *Proceedings of the Royal Society A: Mathematical, Physical and Engineering Sciences* 480.2292 (2024).
- [35] R.B. Randall. *Vibration-based Condition Monitoring: Industrial, Automotive and Aerospace Applications*. Wiley, 2021. URL: <https://books.google.co.uk/books?id=InoqEAAAQBAJ>.
- [36] Robert B Randall et al. “Rolling element bearing diagnostics—A tutorial”. In: *Mechanical systems and signal processing* 25.2 (2011), pp. 485–520.
- [37] Robert B Randall et al. “The relationship between spectral correlation and envelope analysis in the diagnostics of bearing faults and other cyclostationary machine signals”. In: *Mechanical systems and signal processing* 15.5 (2001), pp. 945–962.
- [38] A. Rezaei. “Fault Detection and Diagnosis on the Rolling Element Bearing”. Thesis. Carleton University, 2007.
- [39] Mike Santora. *Schaeffler’s asymmetric spherical roller bearing for wind turbines*. 2017. URL: <https://www.bearingtips.com/schaefflers-asymmetric-spherical-roller-bearing-wind-turbines/>.
- [40] Nader Sawalhi et al. “The enhancement of fault detection and diagnosis in rolling element bearings using minimum entropy deconvolution combined with spectral kurtosis”. In: *Mechanical Systems and Signal Processing* 21.6 (2007), pp. 2616–2633.
- [41] Alexander D Shaw et al. “Normal form analysis of bouncing cycles in isotropic rotor stator contact problems”. In: *International Journal of Mechanical Sciences* 155 (2019), pp. 83–97.
- [42] Sarabjeet Singh et al. “An extensive review of vibration modelling of rolling element bearings with localised and extended defects”. In: *Journal of Sound and Vibration* 357 (2015), pp. 300–330.
- [43] Sarabjeet Singh et al. “Analyses of contact forces and vibration response for a defective rolling element bearing using an explicit dynamics finite element model”. In: *Journal of Sound and Vibration* 333.21 (2014), pp. 5356–5377.
- [44] Jyoti Kumar Sinha. *Industrial approaches in vibration-based condition monitoring*. CRC Press, 2020.